1 **Tidal behavior of a well in a relatively thick semiconfined aquifer**

2 **Xunfeng Lu[1], Kozo Sato[1,2*], and Roland N. Horne[1*]**

3 [1]Department of Energy Science and Engineering, Stanford University, Stanford, CA, USA,
4 [2]Graduate School of Engineering, The University of Tokyo, Tokyo, Japan
5 [*]Corresponding author: Roland N. Horne (horne@stanford.edu); Kozo Sato (sato@frcer.t.u-
6 tokyo.ac.jp)

7
8
9 **Key Points:**

10 • Solutions for tidal responses were derived for both vertical and horizontal wells situated in a
11   relatively thick semiconfined aquifer.

12 • A nondimensional number was derived mathematically, forming the basis for the criterion to
13   assess the validity of the existing solutions.

14 • The new solution was applied to the case of the Arbuckle aquifer to demonstrate the
15   improved validity of the new solution.

16
17

18 **Abstract**

19 Subsurface tidal analysis requires only continuous pressure monitoring data and therefore can be a
20 cost-effective technique for estimating aquifer properties. The tidal behavior of a well in a
21 semiconfined aquifer can be described by a diffusion equation that includes a leakage term. This
22 approach is valid for thin aquifers, as long as the overlying layer has low permeability relative to the
23 main aquifer. However, in cases where the aquifer is not thin and the permeability of the overlying
24 layer is not low, using the existing solutions based on these approximations may lead to unsatisfactory
25 outcomes. Alternative solutions for both vertical and horizontal wells were obtained by solving the
26 standard diffusion equation, with leakage expressed as a boundary condition. Furthermore, a
27 nondimensional number was derived mathematically, which forms the basis for a quantitative criterion
28 to assess the applicability of the existing solutions. In the case of a vertical well, the existing solution
29 exhibits acceptable error only if the nondimensional number is less than 0.245. Our new solution
30 extends this upper limitation to 0.475. However, when the number is greater than 0.475, both the
31 existing solution and our new solution are invalid due to the invalid uniform flowrate assumption. For
32 a horizontal well, when the number is less than 0.245, the existing solution is suitable with acceptable
33 error. Our new solution effectively overcomes this limitation. Finally, the new solution was applied to
34 the case of the Arbuckle aquifer to demonstrate the improved validity of the new solution compared to
35 the existing one.

36 **1. Introduction**

37 **1.1 Earth tides and its application**

38   Earth tides are the deformation of the solid Earth's surface caused by the gravitational attraction
39 of the Moon and the Sun. The gravitational pull of these celestial bodies causes a tidal force on the
40 Earth, which results in the deformation of the Earth's surface, primarily in the form of vertical
41 displacement. The magnitude and phase of the Earth tides vary according to the positions of the Moon
42 and the Sun in relation to the Earth (Melchior, 1966). Earth tides can be calculated by theoretical Earth
43 model given the location and time (Matsumoto, et al., 2001; Agnew, 2012).

44   Earth tides are naturally occurring and offer an opportunity to infer subsurface information.
45 The downhole pressure in closed wells or water level in open wells may include periodic signals with
46 dominantly diurnal and semidiurnal periods induced by Earth tides. Analyzing these oscillatory signals
47 enables the evaluation of various aquifer properties, such as permeability, wellbore storage, skin effect,
48 and CO_2 saturation, by calculating the phase difference and amplitude ratio between the recorded
49 pressure/water level fluctuations and the corresponding theoretical tides (Bredehoeft, 1967; Robinson
50 & Bell, 1971; Gieske & De Vries, 1985; Merritt, 2004; Doan et al., 2006; Cutillo & Bredehoeft, 2011;
51 McMillan et al., 2019; Simon et al., 2021; Liang et al., 2022).

52 **1.2 Tidal response models of confined and semiconfined aquifers to Earth tides**

53   The study of how confined aquifers respond to Earth tides has a rich history and yields valuable
54 information about aquifers. Key analysis parameters include amplitude ratio and phase difference.
55 Amplitude ratio, the ratio between response tidal signals and theoretical tides, can provide insight into
56 the poroelastic properties of the aquifer, including Skempton's coefficient, pore compressibility, and
57 CO_2 saturation. Analyzing the amplitude ratio has been explored in previous studies by Jacob (1939),

58   Arditty et al. (1978), Van der Kamp & Gale (1983), Rojstaczer & Agnew (1989), Wang (1993), Dean

59   et al. (1994), Sato (2006), Burbey (2010), Burbey et al. (2012), Sato & Horne (2018), and Sato et al.

60   (2022). On the other hand, the phase difference between tidal responses and theoretical tides is more

61   closely related to the flow properties of the aquifer, such as permeability, transmissivity, and skin effect,

62   as seen in previous studies like Hsieh et al. (1987), Xue et al. (2013), Lai et al. (2014), Wang et al.

63   (2018), Gao et al. (2020), Zhu & Wang (2020), Zhang et al. (2021), and Lu et al. (2022).

64   While extensive research has been conducted on the tidal behavior of confined aquifers, studies

65   of tidal behavior within semiconfined aquifers have been fewer. In a semiconfined aquifer, flow occurs

66   both from the aquifer to wells and at the interface between the aquifer and the permeable layer above

67   it, known as an aquitard. Recognizing that many aquifers may not be perfectly confined, the

68   consideration of leakage is essential in these semiconfined systems. Such consideration contributes to

69   the safety monitoring of groundwater resources, the security of underground repositories, and the

70   detection of CO_2 leakage. Allègre et al. (2016) utilized a vertical flow model to infer permeability from

71   tidally induced water level variations, without accounting for horizontal flow. Their findings,

72   compared with conventional large-scale pumping tests, revealed consistent hydraulic properties. Wang

73   et al. (2018) expanded upon Hsieh's model (Hsieh et al., 1987) by introducing the concept of specific

74   leakage to the diffusion equation as a volumetric source term and then presented a model for

75   understanding the tidal response in a vertical well to Earth tides in aquifers with both horizontal flow

76   and vertical leakage. Provided that transmissivity and storativity are determined independently, this

77   model can be employed to estimate aquitard leakage by analyzing the phase shift and amplitude ratio.

78   The authors put this model into practice in a US Geological Survey deep monitoring well located in

79   the Arbuckle aquifer in Oklahoma, with their analysis highlighting significant leakage at the site. Gao

80   et al. (2020) proposed new models based on work by Hsieh et al. (1987) and Wang et al. (2018) for

81   tidal analysis that incorporate skin and wellbore storage effects. These models are designed for

82   application to vertical wells situated in confined aquifers with only horizontal flow or in semiconfined

83   aquifers with both horizontal and vertical flow. Capable of accurately assessing information related to

84   aquifers through tidal analysis, the proposed models were tested and validated using real-world

85   examples in both confined and semiconfined aquifers, thereby showcasing their practical applications.

86   Lu et al. (2022) derived and solved tidal response models for analyzing tidal response in a horizontal

87   well, considering factors such as skin effect and wellbore storage across three traditional types of

88   aquifers: confined, semiconfined, and those with mixed boundaries. The authors conducted a variable

89   condition analysis to investigate how different parameters, including wellbore storage, skin effect, and

90   vertical leakage, impact the tidal behavior.

91   It is noted that one of the main assumptions made in previous tidal response models of a

92   semiconfined aquifer is that the overlaying layer has significantly lower hydraulic conductivity than

93   the main aquifer (not an unreasonable assumption in nature). Consequently, leakage from the main

94   aquifer is assumed to be uniformly distributed along the thickness of the main aquifer if it is relatively

95   thin (not always a good assumption in nature because many aquifers are not relatively thin). This

96   simplification replaces the actual flow system with a hypothetical one involving an impermeable

97   confined aquifer, and a diffusion equation incorporating the effect of leakage as a volumetric source

98   term is derived to approximate the flow in such leaky systems (Hantush, 1960; Wang et al., 2018; Gao

99   et al., 2020; Lu et al., 2022). However, this model may not be accurate for systems where the main

100 aquifers are not relatively thin and the permeabilities of the overlaying layer are not relatively low, and

101   in those cases, the standard diffusion equation with leakage expressed as a boundary condition should
102   be used for a more precise mathematical analysis. Hantush (1967) derived such a model where the
103   standard diffusion equation was solved with leakage expressed as a boundary condition to analyze the
104   pump test results. Then, a quantitative criterion was established for the applicability of the solutions
105   that were used in the analysis of pump test. However, the study did not take the tidal force into
106   consideration, which means the author did not incorporate tidal stress term in the diffusion equation.
107   Such types of solutions and quantitative analyses remain an unexplored domain within the field of
108   subsurface tidal analysis. Another assumption made in the previous tidal response models is the
109   uniform flow rate along the wellbore. The quantitative criterion to assess the validity of this assumption
110   should also be analyzed.

111   In this study, new tidal response models of a semiconfined aquifer were derived and solved
112   with leakage expressed as a boundary condition, as it happens naturally in the physical system. Well
113   arrangements (vertical well and horizontal well), skin effect, and wellbore storage are both considered
114   in the new models. Moreover, comparisons with existing solutions were analyzed and a quantitative
115   criterion was established to determine the suitability of the existing solutions derived from the
116   approximate theory that is currently in use and to assess the validity of uniform flow rate assumption
117   quantitatively. Finally, the application of the new model was demonstrated with real-world examples
118   based on previous work by Wang et al. (2018) and Gao et al. (2020).

119   **2. Tidal response model for a vertical well in a semiconfined aquifer**

120   Vertical wells are very common in water resources utilization and oil and gas industries. This
121   section describes the development of a tidal response model for a vertical well in a semiconfined
122   aquifer with skin and wellbore storage considered and with leakage expressed on the boundary
123   condition. A schematic of a vertical well placed in a semiconfined aquifer system is shown in Figure
124   1. The target aquifer is located beneath a permeable aquitard, and above the permeable aquitard is an
125   unconfined aquifer. r_w is the wellbore radius. h and b' are the thickness of the aquifer and permeable
126   aquitard respectively. r_s is the radius of damaged zone that causes the skin effect and the pressure
127   drop at the wellbore caused by skin effect is Δp_s. The definition of the skin factor is $S =$
128    $\left. \Delta p_s \middle/ (r \frac{\partial p}{\partial r})_{r=r_w} \right.$, where pressure p represents the excess pressure in the aquifer above the initial

129   baseline pressure. The assumptions for this model are as follows: (1) both the aquifer and aquitard are
130   laterally infinite; (2) the permeable aquitard has negligible storage and is incompressible; (3) the
131   aquifer and aquitard are isotropic and homogeneous; (4) flow rate is uniform along the wellbore.
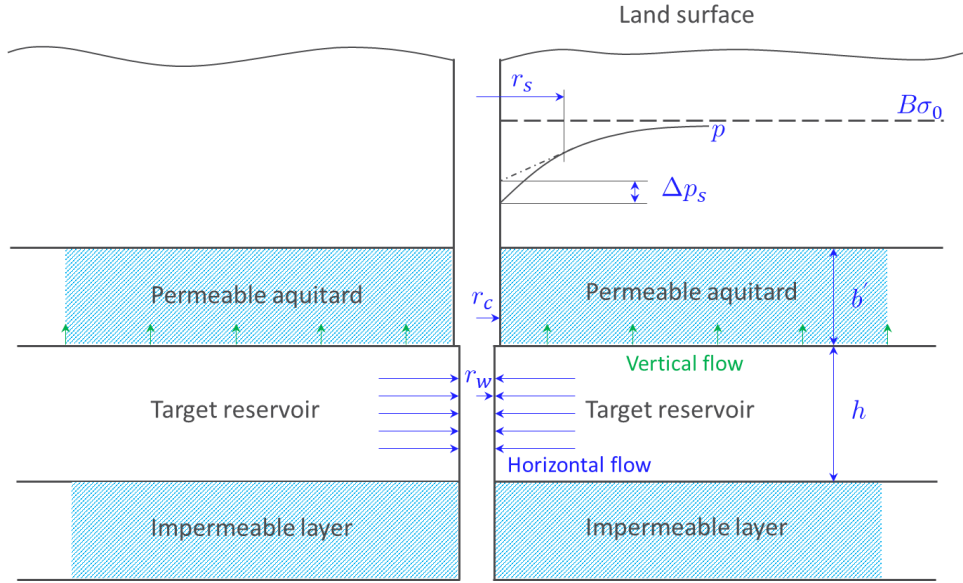
Figure 1: A vertical well placed in a semiconfined aquifer system.

Then the flow transient for a vertical well in a semiconfined aquifer system like Figure 1 under the cubic tidal stress σ_t is governed by:

$$\frac{\partial^2 p}{\partial x^2} + \frac{\partial^2 p}{\partial y^2} + \frac{\partial^2 p}{\partial z^2} = \frac{1}{\eta}\left(\frac{\partial p}{\partial t} - B\frac{\partial \sigma_t}{\partial t}\right), \text{ here } \eta = \frac{k}{\phi\mu C_t} \tag{1.}$$

Here, p equal to $p(m,t)$ is the excess pressure at point m in the aquifer above the initial baseline pressure, so $p(m,t) = p_{absolute} - p_{initial}$. The hydraulic conductivity of the aquifer is $\eta = {k}/{\phi\mu c_t}$ where k, ϕ, μ, and c_t are permeability, porosity, fluid viscosity, and total compressibility respectively. B is the Skempton coefficient, which is defined as the ratio of the change of pore pressure to the change of stress loading under undrained conditions (Skempton, 1954; Wang, 2000).

The initial condition is $p(m,t)|_{t=0} = 0$. The outer boundary conditions at $x = \pm\infty$ and $y = \pm\infty$ are

$$p(m,t)|_{x=\pm\infty, y=\pm\infty} = B\sigma_t \tag{2.}$$

The inner boundary at the wellbore is a flow rate boundary. Considering the effect of skin and wellbore storage, inner boundaries are governed by:

$$q(t) = \frac{2\pi kh}{\mu}\left(r\frac{\partial p}{\partial r}\right)_{r=r_w} = C\frac{dp_w}{dt}, \quad p_w = \left[p - S\frac{q(t)\mu}{2\pi kh}\right]_{r=r_w} \tag{3.}$$

Here, $q(t)$ is the flow rate from the aquifer into the wellbore, named the sand face flow rate. This boundary condition means that the sand face flow rate is equal to the wellbore flow. C is the wellbore storage caused by fluid expansion or changing liquid level. For a fluid expansion storage coefficient, $C = c_w V_w$, where V_w is the volume of the wellbore, and c_w is the compressibility includes the volume changes in the tubing and casing. For a falling liquid level storage coefficient, $C = \frac{A_w}{\rho g}$, where

153   A_w is the cross-sectional area of the wellbore in the region where the liquid level is falling (Horne,
154   1995). S is skin effect and p_w is the pressure measured inside the wellbore.

155   The boundary condition at $z = 0$ is an impermeable boundary, which is

156
$$\left.\frac{\partial p}{\partial z}\right|_{z=0} = 0 \tag{4.}$$

157   The boundary condition at $z = h$ is a permeable boundary, which is a Robin boundary as

158
$$\left.\frac{k'}{\mu b'}p\right|_{z=h} + \left.\frac{k}{\mu}\frac{\partial p}{\partial z}\right|_{z=h} = 0 \tag{5.}$$

159   This boundary is the main point of departure from previous research (Hantush, 1960; Wang et al., 2018;
160   Gao et al., 2020; Lu et al., 2022), where researchers modeled the leakage from the aquifer to the
161   permeable aquitard as a volumetric source term in the diffusion equation and then the semiconfined
162   aquifer is simplified as a confined aquifer and the permeable boundary degenerates into an
163   impermeable boundary. The discussion and analysis in this article mainly revolve around the changes
164   to this boundary condition.

165   **2.1 Helper function: solution of a point source**

166   To solve the governing equation (Equation 1) associated with boundary conditions Equation 2
167   – Equation 5, we can define a helper function, the solution of a point source in the same aquifer system
168   and then integrate the helper function along the z direction from $z = 0$ to $z = h$ to obtain the final
169   solution for the tidal behavior of a vertical well in a semiconfined aquifer. The helper model is shown
170   in Figure 2 (Thambynayagam, 2011). An infinite continuum in the regions $-\infty < x < \infty, -\infty < y <$
171   ∞ and finite in the region $0 < z < h$. Point source at $S_p \equiv (x_0, y_0, z_0)$ at time $t = t_0$ and $-\infty <$
172     $x_0 < \infty, -\infty < y_0 < \infty, 0 < z_0 < d, t_0 \geq 0$. The initial pressure $p(x, y, z, 0) = 0$. The bottom
173   boundary is a Neumann boundary, and the top boundary is a Robin boundary, which are same as
174   Equation 4 and Equation 5. The outer boundaries at $x = \pm\infty$ and $y = \pm\infty$ are also the same as
175   Equation 2.
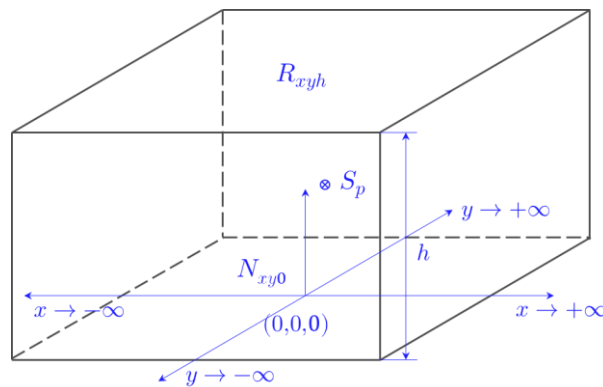

176

177   **Figure 2**: Helper model: pressure transient induced by a point source (from Thambynayagam, 2011).

178   The assumption is made that the flow rate is uniform along the wellbore, so in the helper model,
179   fluid is produced at the rate of $q_s(t) = q(t)/h$ from $t = t_0$ to $t = t$ at a point (x_0, y_0, z_0). The
180   pressure at point m and time t induced by point source S_p, denoted as $p_s(m, t)$, can be obtained

181   by solving the partial differential equation:

182   $$\frac{\partial p_s}{\partial t} - B\frac{\partial \sigma_t}{\partial t} = \eta_x \frac{\partial^2 p_s}{\partial x^2} + \eta_y \frac{\partial^2 p_s}{\partial y^2} + \eta_z \frac{\partial^2 p_s}{\partial z^2} + U(t - t_0)\frac{q(t - t_0)}{\phi c_t h}\delta(x - x_0)\delta(y - y_0)\delta(z - z_0) \quad (6.)$$

183   Associated with initial condition and boundary conditions:

184
$$\begin{cases} p_s(m,t)|_{t=0} & = 0 \\ p_s(m,t)|_{x=\pm\infty, y=\pm\infty} & = B\sigma_t \\ \left.\frac{\partial p_s}{\partial z}\right|_{z=0} & = 0 \\ \left.\frac{k'}{\mu b'}p_s\right|_{z=h} + \left.\frac{k}{\mu}\frac{\partial p_s}{\partial z}\right|_{z=h} & = 0 \end{cases} \quad (7.)$$

185   where $U(t - t_0)$ is Heaviside step function and $\delta(x - x_0)$ is delta function.

186   **2.2 Nondimensional form of the helper model and its solution**

187   The nondimensional equations are posed through the following definitions:

188
$$\begin{aligned} p_{sD} &= \frac{2\pi k h p_s}{\mu} & B\sigma_D &= \frac{2\pi k h B\sigma_t}{\mu} & t_D &= \frac{kt}{\phi\mu c_t(r_w)^2} & C_D &= \frac{C}{2\pi h\phi c_t(r_w)^2} \\ r_D &= \frac{r}{r_w} & x_D &= \frac{x}{r_w} & y_D &= \frac{y}{r_w} & z_D &= \frac{z}{r_w} \end{aligned} \quad (8.)$$

189   If $\eta = \eta_x = \eta_y = \eta_z$ and set $\overline{p_{sD}} = p_{sD} - B\sigma_D$, the nondimensional equation becomes:

190   $$\frac{\partial \overline{p_{sD}}}{\partial t_D} = \frac{\partial^2 \overline{p_{sD}}}{\partial x_D^2} + \frac{\partial^2 \overline{p_{sD}}}{\partial y_D^2} + \frac{\partial^2 \overline{p_{sD}}}{\partial z_D^2} + 2\pi \frac{q_D(t_D - t_{D0})}{r_w}\delta(x_D - x_{D0})\delta(y_D - y_{D0})\delta(z_D - z_{D0}) \quad (9.)$$

191   Associated with boundary conditions:

192
$$\begin{cases} \overline{p_{sD}}|_{t=0} & = 0 \\ \overline{p_{sD}}|_{x=\pm\infty, y=\pm\infty} & = 0 \\ \left.\frac{\partial \overline{p_{sD}}}{\partial z_D}\right|_{z_D=0} & = 0 \\ \left.\frac{\partial \overline{p_{sD}}}{\partial z_D}\right|_{z_D=\frac{h}{r_w}} + \left.\frac{k'}{kb_D}\overline{p_{sD}}\right|_{z_D=\frac{h}{r_w}} & = -\frac{k'}{kb_D}B\sigma_D \end{cases} \quad (10.)$$

193   The next step is to take the Laplace transform of Equation 9 and Equation 10 for t. The Laplace

194   transformation of function $f(t)$ is $\overline{f(s)} = \int_0^\infty f(t)e^{-st}dt$. Here the Laplace variable is s. We have

195   the following equation:

196   $$s\overline{p_{sD}} = \frac{\partial^2 \overline{p_{sD}}}{\partial x_D^2} + \frac{\partial^2 \overline{p_{sD}}}{\partial y_D^2} + \frac{\partial^2 \overline{p_{sD}}}{\partial z_D^2} + 2\pi \frac{q_D(s)\exp(-st_{D0})}{r_w}\delta(x_D - x_{D0})\delta(y_D - y_{D0})\delta(z_D - z_{D0}) \quad (11.)$$

197   We then twice take the complex Fourier transformations of Equation 11 and associated

198   boundary conditions for x and y. The complex Fourier transformation of function $f(x)$ is defined

199   by $\overline{f(x)} = \int_{-\infty}^{+\infty} f(x)e^{imx}\,dx$. We have the following equation:

200   $$s\overline{\overline{\overline{p_{sD}}}} = -m^2\overline{\overline{p_{sD}}} - n^2\overline{\overline{p_{sD}}} + \frac{\partial^2 \overline{\overline{p_{sD}}}}{\partial z_D^2} + 2\pi \frac{q_D(s)\exp(-st_{D0})}{r_w}\delta(z_D - z_{D0})\exp(imx_{D0})\exp(iny_{D0}) \quad (12.)$$

201   Here, m and n are Fourier variables of x and y respectively.

202   We then take (once) the finite Fourier transformation for z of Equation 12 and associated

203   boundary conditions. For the diffusion system $p(x,t) = f(x)T(t)$ with known and time-dependent

204   Neumann boundary $\partial p(0,t)/\partial x$ and Robin boundary $\partial p(h,t)/\partial x + \lambda p(h,t)$, the finite Fourier

205   transformation of function $f(x)$ is:

206   $$\overline{f(\xi_n)} = \int_0^h f(x)\cos(\xi_n x)\,dx \quad (13.)$$

207   and its inversion formula:

208   $$f(x) = 2\sum_{n=1}^{\infty}\overline{f(\xi_n)}\left\{\frac{\xi_n^2 + \lambda^2}{h(\xi_n^2 + \lambda^2) + \lambda}\right\}\cos(\xi_n x) \quad (14.)$$

209   Here ξ_n is a positive root of $\xi_n\tan(\xi_n h) = \lambda, n = 1,2,\dots$.

210   The finite Fourier cosine transform of the second derivative is obtained by integration by parts:

211   $$\int_0^h \frac{\partial^2 p(x,t)}{\partial x^2}\cos(\xi_n x)\,dx = -\xi_n^2\bar{p}(\xi_n,t) - \frac{\partial p(0,t)}{\partial x} + \left\{\frac{\partial p(h,t)}{\partial x} + \lambda p(h,t)\right\}\cos(\xi_n h) \quad (15.)$$

212   After finite Fourier transformation, we have:

213   $$s\overline{\overline{\overline{p_{sD}}}} = -m^2\overline{\overline{\overline{p_{sD}}}} - n^2\overline{\overline{\overline{p_{sD}}}} - \xi_{nD}^2\frac{\partial^2\overline{\overline{p_{sD}}}}{\partial z_D^2} + 2\pi\frac{q_D(s)\exp(-st_{D0})}{r_w}\cos(\xi_{nD}z_{D0})\exp(imx_{D0})\exp(iny_{D0}) - \frac{k'}{kb_D}\overline{\overline{\overline{B\sigma_D}}}\cos(\xi_{nD}h_D) \quad (16.)$$

214   Here, ξ_{nD} is a positive root of $\xi_{nD}\tan(\xi_{nD}h_D) = \lambda_D,\ \lambda_D = k'/kb_D$.

215   Simplifying Equation 16:

216   $$\overline{\overline{\overline{p_{sD}}}} = \frac{1}{r_w}\frac{2\pi q_D(s)\exp(-st_{D0})\cos(\xi_{nD}z_{D0})\exp(imx_{D0})\exp(iny_{D0})}{s + m^2 + n^2 + \xi_{nD}^2} + \frac{-\frac{k'}{kb_D}\overline{\overline{\overline{B\sigma_D}}}\cos(\xi_{nD}h_D)}{s + m^2 + n^2 + \xi_{nD}^2} \quad (17.)$$

217   Dividing Equation 17 into two parts p_{sD1}, the first term of p_{sD} that represents the pressure

218   distribution induced by flow at the point source and p_{sD2}, the second term of p_{sD} that represents the

219   pressure distribution induced by the boundary, then taking the inverse Fourier transformation for m

220   and n:

221
$$\overline{\overline{p_{sD1}}} = \frac{1}{r_w} q_D(s) \exp(-st_{0D}) \cos(\xi_{nD}z_{0D}) K_0\left(\sqrt{((x_{0D}-x_D)^2 + (y_{0D}-y_D)^2)(s+\xi_{nD}^2)}\right) \quad (18.)$$

222
$$\overline{\overline{p_{sD2}}} = -\lambda_D \overline{B\sigma_D} \cos(\xi_{nD}h_D) \frac{1}{s+\xi_{nD}^2} \quad (19.)$$

223   Taking the inverse finite Fourier transformation for ξ_{nD} by Equation 14:

224
$$\overline{p_{sD1}} = \frac{2}{r_w} q_D(s) \exp(-st_{0D}) \sum_{n=1}^{\infty} \cos(\xi_{nD}z_{0D}) \cos(\xi_{nD}z_D) \frac{\xi_{nD}^2 + \lambda_D^2}{h_D(\xi_{nD}^2 + \lambda_D^2) + \lambda_D} K_0\left(\sqrt{((x_{0D}-x_D)^2 + (y_{0D}-y_D)^2)(s+\xi_{nD}^2)}\right) (20.)$$

225
$$\overline{p_{sD2}} = -2\sum_{n=1}^{\infty} \lambda_D \overline{B\sigma_D} \cos(\xi_{nD}h_D) \frac{1}{s+\xi_{nD}^2} \frac{\xi_{nD}^2 + \lambda_D^2}{h_D(\xi_{nD}^2 + \lambda_D^2) + \lambda_D} \cos(\xi_{nD}z_D) \quad (21.)$$

226   **2.3 The solution of the vertical well with wellbore storage and skin effect considered**

227   The solution of a vertical well in Laplace space $\overline{p_D}$ can be obtained by firstly, integrating $\overline{p_{sD1}}$
228   along the wellbore direction from $z_0 = 0$ to $z_0 = h$ to obtain $\overline{p_{D1}}$, and secondly, $\overline{p_{D2}} = \overline{p_{sD2}}$. Then,
229    $\overline{p_D} = \overline{p_{D1}} + \overline{p_{D2}}$. The result of $\overline{p_{D1}}$ is shown here:

230
$$\overline{p_{D1}} = 2q_D(s) \exp(-st_{0D}) \sum_{n=1}^{\infty} \cos(\xi_{nD}z_D) \frac{1}{\xi_{nD}} \sin(\xi_{nD}h_D) \frac{\xi_{nD}^2 + \lambda_D^2}{h_D(\xi_{nD}^2 + \lambda_D^2) + \lambda_D}$$
$$K_0\left(\sqrt{((x_{0D}-x_D)^2 + (y_{0D}-y_D)^2)(s+\xi_{nD}^2)}\right) \quad (22.)$$

231   Wellbore storage and skin effect can be easily introduced into the final solution via $q_D(s)$ (the
232   details can be found in Lu et al. (2022)) and finally the transfer function between $\overline{p_{wD}}$ (the
233   nondimensional pressure at the wellbore) and the theoretical pressure induced by theoretical Earth tidal
234   stress $\overline{B\sigma_D}$ is:

235
$$\begin{aligned}
H(s) &= \frac{\bar{B}+1}{1 + C_D S s + C_D s^2 A} \\
\bar{B} &= -2\sum_{n=1}^{\infty} \frac{(\xi_{nD}^2 + \lambda_D^2)}{h_D(\xi_{nD}^2 + \lambda_D^2) + \lambda_D} \frac{\lambda_D}{s+\xi_{nD}^2} \cos(\xi_{nD}z_D)\cos(\xi_{nD}h_D) \\
A &= \frac{2}{s}\sum_{n=1}^{\infty} \frac{(\xi_{nD}^2 + \lambda_D^2)}{h_D(\xi_{nD}^2 + \lambda_D^2) + \lambda_D} K_0\left(\sqrt{((x_{0D}-x_D)^2 + (y_{0D}-y_D)^2)(s+\xi_{nD}^2)}\right) \cos(\xi_{nD}z_D) \frac{1}{\xi_{nD}} \sin(\xi_{nD}h_D)
\end{aligned} \quad (23.)$$

236   **3. Tidal response model for a horizontal well in a semiconfined aquifer**

237   Horizontal wells have been used in many applications, including oil and gas production,
238   geothermal extraction, hazardous waste remediation, and CO_2 sequestration. In this section, a tidal
239   response model for a horizontal well in a semiconfined aquifer is developed with skin and wellbore
240   storage considered and with leakage expressed on the boundary condition. A schematic of a horizontal
241   well living in a semiconfined aquifer system is shown in Figure 3. Notations are the same as in Section
242   2 for a vertical well, in addition to L representing the length of a horizontal well. The same
243   assumptions are made as follows: (1) both the aquifer and aquitard are laterally infinite; (2) the

244 permeable aquitard has negligible storage and is incompressible; (3) the aquifer and aquitard are
245 isotropic and homogeneous; (4) flow rate is uniform along the wellbore.
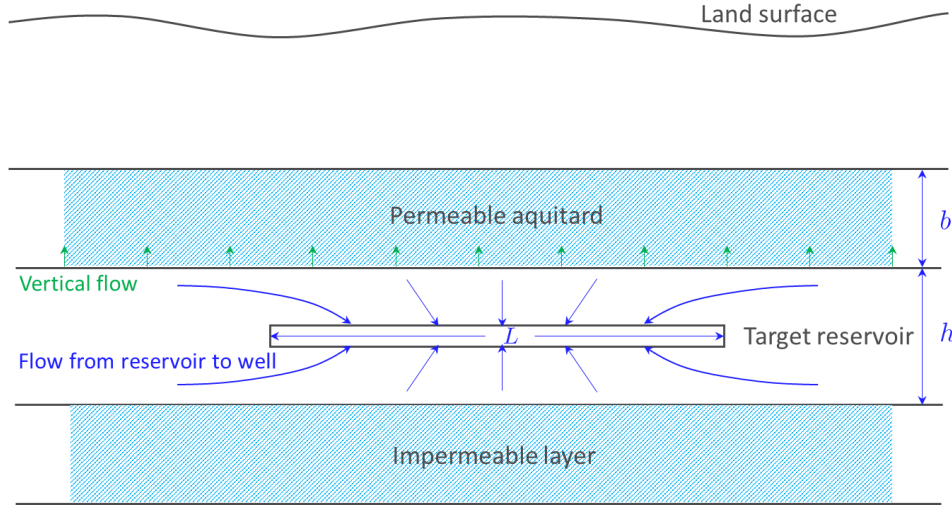
246

247 **Figure 3**: A horizontal well living in a semiconfined aquifer system.

248   Then the flow transient for a horizontal well in a semiconfined aquifer system like Figure 3
249 under the cubic tidal stress σ_t is governed by the same governing equation and the same boundary
250 conditions posed previously for a vertical well in a semiconfined aquifer system:

$$\frac{\partial^2 p}{\partial x^2} + \frac{\partial^2 p}{\partial y^2} + \frac{\partial^2 p}{\partial z^2} = \frac{1}{\eta}\left(\frac{\partial p}{\partial t} - B\frac{\partial \sigma_t}{\partial t}\right), \text{ here } \eta = \frac{k}{\phi\mu C_t} \tag{24.}$$

251

$$\begin{cases} p(m,t)|_{t=0} &= 0 \\ p(m,t)|_{x=\pm\infty,y=\pm\infty} &= B\sigma_t \\ \left.\frac{\partial p}{\partial z}\right|_{z=0} &= 0 \\ \left.\frac{k'}{\mu b'}p\right|_{z=h} + \left.\frac{k}{\mu}\frac{\partial p}{\partial z}\right|_{z=h} &= 0 \\ p_w &= \left[p - S\frac{q(t)}{2\pi kh}\right]_{r=r_w} \\ q(t) &= \frac{2\pi kh}{\mu}\left(r\frac{\partial p}{\partial r}\right) = C\frac{dp_w}{dt} \end{cases}$$

252

253 It is noted that leakage is expressed as a boundary condition instead of expressed as a volumetric source
254 term in the diffusion equation as in earlier research.

255   **3.1 Helper function: solution of a point source**

256   To solve the governing equation associated with boundary conditions Equation 24, we use the
257 same helper model as shown in Figure 2 (described in Section 2) and solve a similar helper function,
258 the solution of a point source in the same aquifer system and then integrate the helper function along
259 the x direction from $x = -L/2$ to $x = L/2$ to obtain the final solution for the tidal behavior of a
260 horizontal well in a semiconfined aquifer. Fluid is produced at the rate of $q_s(t) = q(t)/L$ from $t = $
261 t_0 to $t = t$ at a point (x_0, y_0, z_0). We solve $p_s(m,t)$, the pressure at point m and time t induced

262   by a point source S_p, from the partial differential equation:

263      $$\frac{\partial p_s}{\partial t} - B\frac{\partial \sigma_t}{\partial t} = \eta_x \frac{\partial^2 p_s}{\partial x^2} + \eta_y \frac{\partial^2 p_s}{\partial y^2} + \eta_z \frac{\partial^2 p_s}{\partial z^2} + U(t-t_0)\frac{q(t-t_0)}{\phi c_t L}\delta(x-x_0)\delta(y-y_0)\delta(z-z_0) \quad (25.)$$

264   Associated with initial condition and boundary conditions:

265
$$\begin{cases} p_s(m,t)|_{t=0} & = 0 \\ p_s(m,t)|_{x=\pm\infty, y=\pm\infty} & = B\sigma_t \\ \left.\dfrac{\partial p_s}{\partial z}\right|_{z=0} & = 0 \\ \left.\dfrac{k'}{\mu b'}p_s\right|_{z=h} + \left.\dfrac{k}{\mu}\dfrac{\partial p_s}{\partial z}\right|_{z=h} & = 0 \end{cases} \qquad (26.)$$

266   where $U(t-t_0)$ is Heaviside step function and $\delta(x-x_0)$ is delta function. It is noted that the slight
267   difference between helper function for a vertical well Equation 6 and helper function for a horizontal
268   well Equation 25 is in the definition of $q_s(t)$. The former one is $q_s(t) = q(t)/h$ and the latter one is
269      $q_s(t) = q(t)/L$.

270   **3.2 Nondimensional form of the helper model and its solution**

271   The nondimensional equations are posed through the following definitions:

272
$$\begin{aligned} p_{sD} &= \frac{2\pi kL p_s}{\mu} & B\sigma_D &= \frac{2\pi kLB\sigma_t}{\mu} & t_D &= \frac{kt}{\phi\mu c_t(L/2)^2} & C_D &= \frac{C}{2\pi L\phi c_t(L/2)^2} \\ r_D &= \frac{r}{L/2} & x_D &= \frac{x}{L/2} & y_D &= \frac{y}{L/2} & z_D &= \frac{z}{L/2} \end{aligned} \qquad (27.)$$

273   If $\eta = \eta_x = \eta_y = \eta_z$ and set $\overline{p_{sD}} = p_{sD} - B\sigma_D$, the nondimensional equation becomes:

274
$$\frac{\partial \overline{p_{sD}}}{\partial t_D} = \frac{\partial^2 \overline{p_{sD}}}{\partial x_D^2} + \frac{\partial^2 \overline{p_{sD}}}{\partial y_D^2} + \frac{\partial^2 \overline{p_{sD}}}{\partial z_D^2} + 4\pi\frac{q_D(t_D-t_{D0})}{L}\delta(x_D-x_{D0})\delta(y_D-y_{D0})\delta(z_D-z_{D0}) \quad (28.)$$

275   Associated with boundary conditions:

276
$$\begin{cases} \overline{p_{sD}}|_{t=0} & = 0 \\ \overline{p_{sD}}|_{x=\pm\infty, y=\pm\infty} & = 0 \\ \left.\dfrac{\partial \overline{p_{sD}}}{\partial z_D}\right|_{z_D=0} & = 0 \\ \left.\dfrac{\partial \overline{p_{sD}}}{\partial z_D}\right|_{z_D=\frac{2h}{L}} + \left.\dfrac{k'}{kb_D}\overline{p_{sD}}\right|_{z_D=\frac{2h}{L}} & = -\dfrac{k'}{kb_D}B\sigma_D \end{cases} \qquad (29.)$$

277   After Laplace transformation of Equation 28 and Equation 29 for t, twice complex Fourier
278   transformations for x and y, and once finite Fourier transformation for z, we have:

279      $$s\overline{\overline{\overline{p_{sD}}}} = -m^2\overline{\overline{\overline{p_{sD}}}} - n^2\overline{\overline{\overline{p_{sD}}}} - \xi_{nD}^2\frac{\partial^2\overline{\overline{\overline{p_{sD}}}}}{\partial z_D^2} + 4\pi\frac{q_D(s)\exp(-st_{D0})}{L}\cos(\xi_{nD}z_{D0})\exp(imx_{D0})\exp(iny_{D0}) - \frac{k'}{kb_D}\overline{\overline{\overline{B\sigma_D}}}\cos(\xi_{nD}h_D) \quad (30.)$$

280   Here, ξ_{nD} is a positive root of $\xi_{nD}\tan(\xi_{nD}h_D) = \lambda_D$, $\lambda_D = {k'}/{kb_D}$.

281   Simplifying Equation 30:

$$
282 \quad \overline{\overline{\overline{p_{sD}}}} = \frac{1}{L} \frac{4\pi q_D(s)\exp(-st_{D0})\cos(\xi_{nD}z_{D0})\exp(imx_{D0})\exp(iny_{D0})}{s + m^2 + n^2 + \xi_{nD}^2} + \frac{-\frac{k'}{kb_D}\overline{\overline{B\sigma_D}}\cos(\xi_{nD}h_D)}{s + m^2 + n^2 + \xi_{nD}^2} \quad (31.)
$$

283   Similarly, dividing Equation 31 into two parts p_{sD1}, the first term of p_{sD} that represents the
284   pressure distribution induced by flow at the point source and p_{sD2}, the second term of p_{sD} that
285   represents the pressure distribution induced by the boundary, then taking the inverse Fourier
286   transformation for m and n and inverse finite Fourier transformation for ξ_{nD}:

$$
287 \quad \overline{p_{sD1}} = \frac{4}{L}q_D(s)\exp(-st_{0D})\sum_{n=1}^{\infty}\cos(\xi_{nD}z_{0D})\cos(\xi_{nD}z_D)\frac{\xi_{nD}^2 + \lambda_D^2}{h_D(\xi_{nD}^2 + \lambda_D^2) + \lambda_D}K_0\left(\sqrt{((x_{0D}-x_D)^2 + (y_{0D}-y_D)^2)(s + \xi_{nD}^2)}\right)(32.)
$$

$$
288 \quad \overline{p_{sD2}} = -2\sum_{n=1}^{\infty}\lambda_D\overline{B\sigma_D}\cos(\xi_{nD}h_D)\frac{1}{s + \xi_{nD}^2}\frac{\xi_{nD}^2 + \lambda_D^2}{h_D(\xi_{nD}^2 + \lambda_D^2) + \lambda_D}\cos(\xi_{nD}z_D) \quad (33.)
$$

289   **3.3 The solution of the horizontal well with wellbore storage and skin effect considered**

290   The solution of a horizontal well in Laplace space $\overline{p_D}$ can be obtained by firstly setting $x =$
291    $y = 0$ and integrate $\overline{p_{sD1}}$ along the wellbore direction from $x_0 = -L/2$ to $x_0 = L/2$ to obtain
292    $\overline{p_{D1}}$. Secondly, $\overline{p_{D2}} = \overline{p_{sD2}}$. Then, $\overline{p_D} = \overline{p_{D1}} + \overline{p_{D2}}$. The result of $\overline{p_{D1}}$ is shown here:

$$
293 \quad \overline{p_{D1}} = 4q_D(s)\exp(-st_{0D})\sum_{n=1}^{\infty}\cos(\xi_{nD}z_{0D})\cos(\xi_{nD}z_D)\frac{\xi_{nD}^2 + \lambda_D^2}{h_D(\xi_{nD}^2 + \lambda_D^2) + \lambda_D}\operatorname{arcsinh}\left(\frac{\pi}{2\sqrt{s + \xi_{nD}^2}}\right)(34.)
$$

294   Similarly, wellbore storage and skin effect can be easily introduced into the final solution via
295    $q_D(s)$ (the details can be found in Lu et al. (2022)) and finally the transfer function between $\overline{p_{wD}}$ (the
296   nondimensional pressure at the wellbore) and the theoretical pressure induced by theoretical Earth tidal
297   stress $\overline{B\sigma_D}$ for a horizontal well is:

$$
298 \quad \begin{aligned}
H(s) &= \frac{\bar{B} + 1}{1 + C_D Ss + C_D s^2 A} \\
\bar{B} &= -2\sum_{n=1}^{\infty}\frac{(\xi_{nD}^2 + \lambda_D^2)}{h_D(\xi_{nD}^2 + \lambda_D^2) + \lambda_D}\frac{\lambda_D}{s + \xi_{nD}^2}\cos(\xi_{nD}z_D)\cos(\xi_{nD}h_D) \\
A &= \frac{4}{s}\sum_{n=1}^{\infty}\frac{(\xi_{nD}^2 + \lambda_D^2)}{h_D(\xi_{nD}^2 + \lambda_D^2) + \lambda_D}\sinh^{-1}\frac{\pi}{2\sqrt{(s + \xi_{nD}^2)}}\cos(\xi_{nD}z_{wD})\cos(\xi_{nD}z_D)
\end{aligned} \quad (35.)
$$

299   **4. Comparison with the existing solutions and the quantitative criteria**

300   In this section, the solved solutions Equation 23 and Equation 35 are compared with the
301   previously available solutions. Also, the quantitative criteria are derived to assess the applicability of
302   the existing solutions and the new solutions.

303   **4.1 Comparison with the existing solution of a vertical well: Gao's model**

304   The transfer function of Gao's model (Gao et al., 2020) for a vertical well living in a

305   semiconfined aquifer is shown as:

$$H(i\omega) = \left[1 + \frac{\alpha_D^2}{2S_D\beta_D}\frac{K_0(\beta_D)}{K_1(\beta_D)} + \pi i\frac{s}{T_D}\right]^{-1}\left(\frac{\alpha_D}{\beta_D}\right)^2 \tag{36.}$$

307   Here, $\alpha_D = r_w\sqrt{\frac{i\omega\phi\mu c_t}{k}} = \sqrt{\frac{2\pi i S_D}{T_D}}$, $S_D = \frac{\pi\phi c_t h r_w^2}{C} = \frac{1}{2C_D}$, $T_D = \frac{2\pi^2 kh}{C\mu\omega} = \frac{\pi\tau kh}{C\mu}$, $\beta_D =$

308    $r_w\sqrt{H' + \frac{i\omega\phi\mu c_t}{k}} = \sqrt{H_D + \alpha_D^2}$, $H' = \frac{K'}{b'T}$ and $H_D = r_w^2 H'$. K' is the vertical hydraulic conductivity

309   of the overlaying aquitard and T is the transmissivity of the target aquifer. Replace $i\omega$ using

310   Laplace variable s, Equation 36 can be rewritten as:

$$H(s) = \frac{B}{1 + C_D S s + C_D s^2 A}$$
$$B = \frac{s}{H_D + s} \tag{37.}$$
$$A = \frac{1}{s\sqrt{(H_D + s)}}\frac{K_0\left(\sqrt{(H_D + s)}\right)}{K_1\left(\sqrt{(H_D + s)}\right)}$$

312   If leakage is expressed on the boundary, the solution for a vertical well has been solved as

313   Equation 23. Equation 23 is placed here again for the convenience of comparison (set $(x_{0D} - x_D)^2 +$

314    $(y_{0D} - y_D)^2 = r_D = 1$, the position at wellbore):

$$H(s) = \frac{\bar{B} + 1}{1 + C_D S s + C_D s^2 A}$$
$$\bar{B} = -2\sum_{n=1}^{\infty}\frac{(\xi_{nD}^2 + \lambda_D^2)}{h_D(\xi_{nD}^2 + \lambda_D^2) + \lambda_D}\frac{\lambda_D}{s + \xi_{nD}^2}\cos(\xi_{nD}z_D)\cos(\xi_{nD}h_D) \tag{38.}$$
$$A = \frac{2}{s}\sum_{n=1}^{\infty}\frac{(\xi_{nD}^2 + \lambda_D^2)}{h_D(\xi_{nD}^2 + \lambda_D^2) + \lambda_D}K_0\left(\sqrt{(s + \xi_{nD}^2)}\right)\cos(\xi_{nD}z_D)\frac{1}{\xi_{nD}}\sin(\xi_{nD}h_D)$$

316   Here, ξ_{nD} is a positive root of $\xi_{nD}\tan(\xi_{nD}h_D) = \lambda_D$, $\lambda_D = k'/kb_D = H_D h_D$.

317   Starting with:

$$h_D\xi_{nD}\tan(\xi_{nD}h_D) = h_D\lambda_D = \left(h_D\sqrt{H_D}\right)^2 \tag{39.}$$

319   We can derive a quantitative criterion for a vertical well model to assess the applicability of the

320   previous models like Gao's and Wang's models (Gao, et al., 2020; Wang, et al., 2018).

321   The first positive root ξ_{0D} is firstly discussed here. The Taylor expansion of $\tan x = x +$

322    $\frac{1}{3}x^3 + O(x^5)$, then Equation 39 becomes if $h_D\xi_{0D}$ is represented by x for the convenience of

323   mathematics:

324
$$x\left(x + \frac{1}{3}x^3 + O(x^5)\right) = \left(h_D\sqrt{H_D}\right)^2 \tag{40.}$$

325 Because $h_D\sqrt{H_D}$ is a small value, x is also small, then:

326
$$\frac{1}{3}x^4 + x^2 - \left(h_D\sqrt{H_D}\right)^2 = 0 \tag{41.}$$

327 The solution of Equation 41 is:

328
$$x^2 = \frac{-1 + \sqrt{1 + \frac{4}{3}\left(h_D\sqrt{H_D}\right)^2}}{\frac{2}{3}} \tag{42.}$$

329 The Taylor expansion of $\sqrt{1+x} = 1 + \frac{x}{2} - \frac{x^2}{8} + O(x^3)$, then Equation 42 can be rewritten as:

330
$$x^2 = \left(h_D\sqrt{H_D}\right)^2 - \frac{1}{3}\left(h_D\sqrt{H_D}\right)^4 + O\left(\left(h_D\sqrt{H_D}\right)^6\right) \tag{43.}$$

331 If a 1% error is acceptable on x, then $\frac{1}{3}\left(h_D\sqrt{H_D}\right)^4$ should be no more than 2% of $\left(h_D\sqrt{H_D}\right)^2$

332 and $x^2 \approx \left(h_D\sqrt{H_D}\right)^2$, which means

333
$$\xi_{0D} \approx \sqrt{H_D} \tag{44.}$$

334 and the quantitative criterion is:

335
$$h_D\sqrt{H_D} < 0.245 \tag{45.}$$

336 For other positive roots ξ_{nD},

337
$$\xi_{nD} \approx n\pi/h_D, n = 1,2,3 \dots \tag{46.}$$

338 Inserting Equation 44 and Equation 46 to Equation 38, which is the solution of the new model,
339 and ignoring small terms, then:

340
$$\overline{B} + 1 \approx \frac{s}{s + H_D} \tag{47.}$$

341 which is the term B in Equation 37, the solution of the previous Gao's model.

342 Additionally, the term A in Equation 38 is approximated as:

343
$$A \approx \frac{K_0\left(\sqrt{s + H_D}\right)}{s} \tag{48.}$$

344   For small arguments $0 < |x| \ll \sqrt{\alpha + 1}$, we have:

345
$$K_\alpha(x) \sim \begin{cases} -ln\left(\dfrac{x}{2}\right) - \gamma & \text{if } \alpha = 0 \\ \dfrac{\Gamma(\alpha)}{2}\left(\dfrac{2}{x}\right)^\alpha & \text{if } \alpha > 0 \end{cases} \qquad (49.)$$

346 So, the term A in Equation 37 can also be simplified given $H_D + s$ is small:

347
$$A \approx \frac{K_0\left(\sqrt{s + H_D}\right)}{s}$$

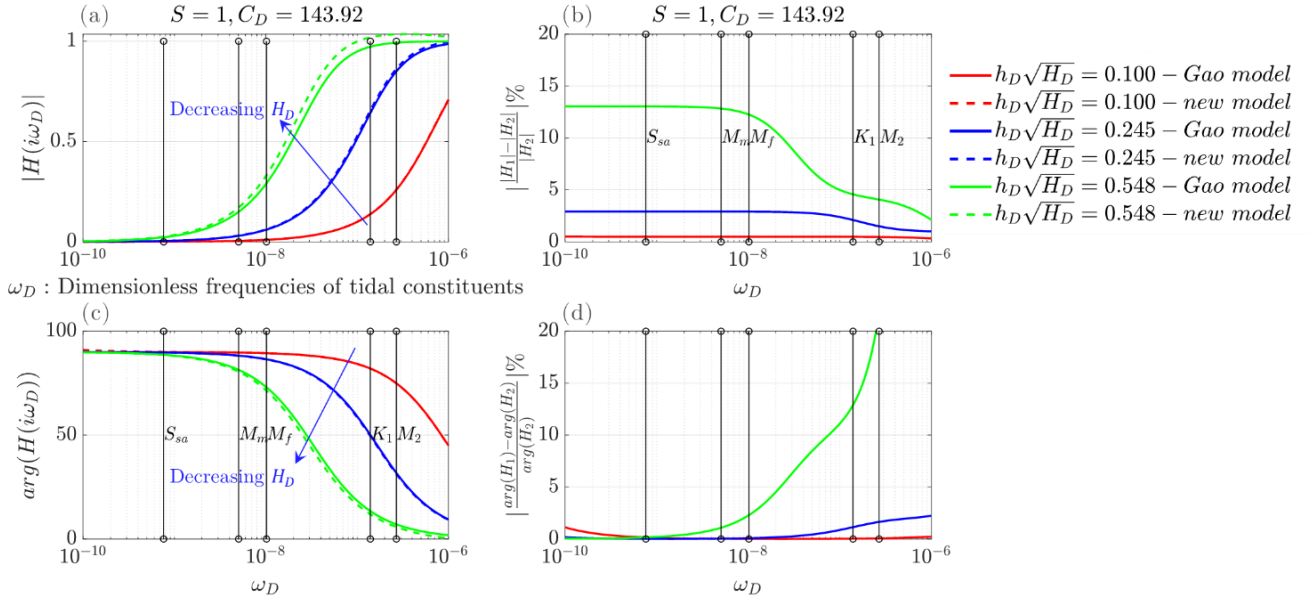348 which is the same as Equation 48, the approximated value of term A in Equation 38.

349   Hence, it is demonstrated that we could derive the solution of the previous Gao's model
350 (Equation 37) from the solution of the new model (Equation 38) given the quantitative criterion

351 $h_D\sqrt{H_D} < 0.245$.

352   Figure 3 illustrates a comparison between Gao's model and the new model under three different

353 values of $h_D\sqrt{H_D}$, ranging from 0.1 to 0.548. The relative error is also examined in the figure. The

354 absolute values of physical parameters to generate Figure 4 are shown in Table 1. Different tidal
355 constituents are marked in the figure and periods of these tidal constituents are listed in Table 2. When

356 $h_D\sqrt{H_D} = 0.1$, the amplitude and phase of transfer function H for Gao's model and new model are

357 almost identical. However, there are larger differences of the amplitude and phase of transfer function

358 H between Gao's model and new model when $h_D\sqrt{H_D} = 0.548$. This means the previous model is

359 not suitable for aquifer with relatively larger $h_D\sqrt{H_D}$. With the increasing frequency, the relative error

360 of amplitude of transfer function between the previous model and new model decreases from more

361 than 12% to less than 5% for $h_D\sqrt{H_D} = 0.548$ while the relative error of phase of transfer function

362 increases rapidly from around 0% to more than 20% for $h_D\sqrt{H_D} = 0.548$. Hence, models should be

363 chosen carefully if the phase difference for semidiurnal tidal constituent and diurnal tidal constituent
364 are analyzed to infer aquifer properties, which is a common method in hydrological applications
365 (McMillan, et al., 2019; Rau, et al., 2022; Valois, et al., 2022).

366   The amplitude ratio and phase difference between water level and tidal force depend on
367 frequencies of tidal force and vertical leakage coefficient H_D. With the increasing frequency of tides,
368 the amplitude ratio increases and phase advance decreases, which means the aquifer tends to be
369 confined aquifer under tidal force with high frequency and tends to be open aquifer under tidal force
370 with low frequency (Wang, 2000). With the decreasing vertical leakage coefficient, the amplitude ratio
371 increases and phase difference decreases, which is reasonable because the aquifer becomes more
372 confined aquifer.

373

374

375 **Figure 4**: Comparison between Gao's model and the new model under three different values of

376 $h_D\sqrt{H_D}$. (a): the amplitude of the transfer functions; (b): the relative error in amplitude of the transfer

377 functions between Gao's solution and the new solution; (c): the phase of the transfer functions; (d)

378 the relative error in phase of the transfer functions between Gao's solution and the new solution. (S_{sa}:

379 semiannual constituent; M_m: monthly constituent; M_f: Fortnightly constituent; K_1: diurnal

380 constituent; M_2: semidiurnal constituent.)

381 **Table 1**: The absolute values of physical parameters to generate Figure 4

Parameters	Values	Parameters	Values
Well radius r_w	0.1 m	Aquifer permeability k	4×10^{-12} m^2
Viscosity μ	0.003 Pa·s	Aquitard permeability	4×10^{-13} m^2
Porosity φ	0.25	Aquitard thickness h	10,60,300 m
Compressibility c_t	1.02×10^{-9} Pa^{-1}	Skin S	1
Aquifer thickness b'	100 m	Wellbore storage C	$2.3059\times10^{-9}\cdot\ h$ m^3

382 **Table 2**: Different tidal constituents and its periods

Tidal constituent	Period
M_2	12.421 h
K_1	23.934 h
M_f	13.661 days
M_m	27.555 days
S_{sa}	0.5 yr

383

384 **4.2 Comparison with the existing solution of a horizontal well: Lu's model**

385 The transfer function of Lu's model (Lu et al., 2022) for a horizontal well living in a

386 semiconfined aquifer is shown as:

387
$$H(s) = \frac{B}{1 + C_D S s + C_D s^2 A}$$

$$B = \frac{s}{s + H_D}$$ (50.)

$$A = \frac{2}{s}\frac{1}{h_D}\sinh^{-1}\frac{\pi}{2\sqrt{s + H_D}} + \frac{4}{s}\sum_{n=1}^{\infty}\frac{1}{h_D}\sinh^{-1}\frac{\pi}{2\sqrt{\left(s + H_D + \left(\frac{n\pi}{h_D}\right)^2\right)}}\cos\frac{n\pi z_{wD}}{h_D}\cos\frac{n\pi z_D}{h_D}$$

388 The solution for a horizontal well if the leakage is expressed in boundary has been solved as
389 Equation 35, which is placed here again for the convenience of comparison:

390
$$H(s) = \frac{\bar{B} + 1}{1 + C_D S s + C_D s^2 A}$$

$$\bar{B} = -2\sum_{n=1}^{\infty}\frac{(\xi_{nD}^2 + \lambda_D^2)}{h_D(\xi_{nD}^2 + \lambda_D^2) + \lambda_D}\frac{\lambda_D}{s + \xi_{nD}^2}\cos(\xi_{nD}z_D)\cos(\xi_{nD}h_D)$$ (51.)

$$A = \frac{4}{s}\sum_{n=1}^{\infty}\frac{(\xi_{nD}^2 + \lambda_D^2)}{h_D(\xi_{nD}^2 + \lambda_D^2) + \lambda_D}\sinh^{-1}\frac{\pi}{2\sqrt{(s + \xi_{nD}^2)}}\cos(\xi_{nD}z_{wD})\cos(\xi_{nD}z_D)$$

391 Here, ξ_{nD} is a positive root of $\xi_{nD}\tan(\xi_{nD}h_D) = \lambda_D$, $\lambda_D = {k'}/{kb_D} = H_D h_D$.

392 It should be noted that for horizontal well and vertical well models, although the symbols used
393 are the same, the characteristic length used for nondimensionalization is different. For the horizontal
394 well model, the characteristic length is half well length ($L/2$), but for the vertical well model, the
395 characteristic length is wellbore radius (r_w).

396 Similarly, starting with $h_D\xi_{nD}\tan(\xi_{nD}h_D) = h_D\lambda_D = \left(h_D\sqrt{H_D}\right)^2$, the quantitative criterion for
397 a horizontal well model can be derived mathematically to assess the applicability of Lu's model (Lu,
398 et al., 2022). The criterion for a horizontal well model is the same with that for a vertical well model:

399 $h_D\sqrt{H_D} < 0.245$, then $\xi_{0D} \approx \sqrt{H_D}$, $\xi_{nD} \approx n\pi/h_D, n = 1,2,3\ ....$

400 Inserting the approximated ξ_{nD} to Equation 51 and ignoring small terms, then:

401
$$\overline{B} + 1 \approx \frac{s}{s + H_D}$$ (52.)

402 which is the term B of the previous Lu's model Equation 50.

403 The term A in Equation 51 is approximated as:

404
$$A \approx \frac{2}{s}\frac{1}{h_D}\sinh^{-1}\frac{\pi}{2\sqrt{s + H_D}} + \frac{4}{s}\sum_{n=1}^{\infty}\frac{1}{h_D}\sinh^{-1}\frac{\pi}{2\sqrt{\left(s + \left(\frac{n\pi}{h_D}\right)^2\right)}}\cos\frac{n\pi z_{wD}}{h_D}\cos\frac{n\pi z_D}{h_D}$$ (53.)

405 Because H_D is small enough compared to $s + \left(\frac{n\pi}{h_D}\right)^2$ given $h_D\sqrt{H_D} < 0.245$, the term A in

406 Equation 50 could be approximated as:

407
$$A \approx \frac{2}{s}\frac{1}{h_D}\sinh^{-1}\frac{\pi}{2\sqrt{s + H_D}} + \frac{4}{s}\sum_{n=1}^{\infty}\frac{1}{h_D}\sinh^{-1}\frac{\pi}{2\sqrt{\left(s + \left(\frac{n\pi}{h_D}\right)^2\right)}}\cos\frac{n\pi z_{wD}}{h_D}\cos\frac{n\pi z_D}{h_D} \qquad (54.)$$

408 which is the same as Equation 53, the approximated value of term A in Equation 51.

409 Similarly, we show that the solution of the previous Lu's model (Equation 50) could be derived

410 from the solution of the new model (Equation 51) given the quantitative criterion $h_D\sqrt{H_D} < 0.245$.

411 Figure 5 provides a comparison between Lu's model and the new horizontal model under three

412 different values of $h_D\sqrt{H_D}$, ranging from 0.1 to 0.548. Within this range, the relative error is also

413 examined. The absolute values of physical parameters used to generate Figure 5 are laid out in Table
414 3. The figure also marks different tidal constituents, with the periods of these tidal constituents detailed

415 in Table 2. When $h_D\sqrt{H_D} = 0.1$, there is a close resemblance between the amplitude and phase of the

416 transfer function for both Lu's model and the new model. However, as $h_D\sqrt{H_D}$ increases to 0.548, a

417 noticeable difference between Lu's model and the new model emerges in the amplitude and phase of
418 the transfer function. This discrepancy implies that the previous model becomes unsuitable for aquifers

419 with relatively larger values of $h_D\sqrt{H_D}$. As the frequency increases, the relative error in amplitude of

420 the transfer function between the previous model and the new model decreases from over 10% to less

421 than 2% for $h_D\sqrt{H_D} = 0.548$. Conversely, the relative error in the phase of the transfer function

422 escalates rapidly from approximately 0% to more than 10% for the same value of $h_D\sqrt{H_D}$. Therefore,

423 selecting the appropriate model requires careful consideration, especially when analyzing the phase
424 difference for semidiurnal tidal constituents and diurnal tidal constituents to infer aquifer properties.
425 In addition, the dependence of amplitude ratio and phase difference between water level and tidal force
426 in a horizontal well on frequencies of tidal force and vertical leakage coefficient H_D is similar to that
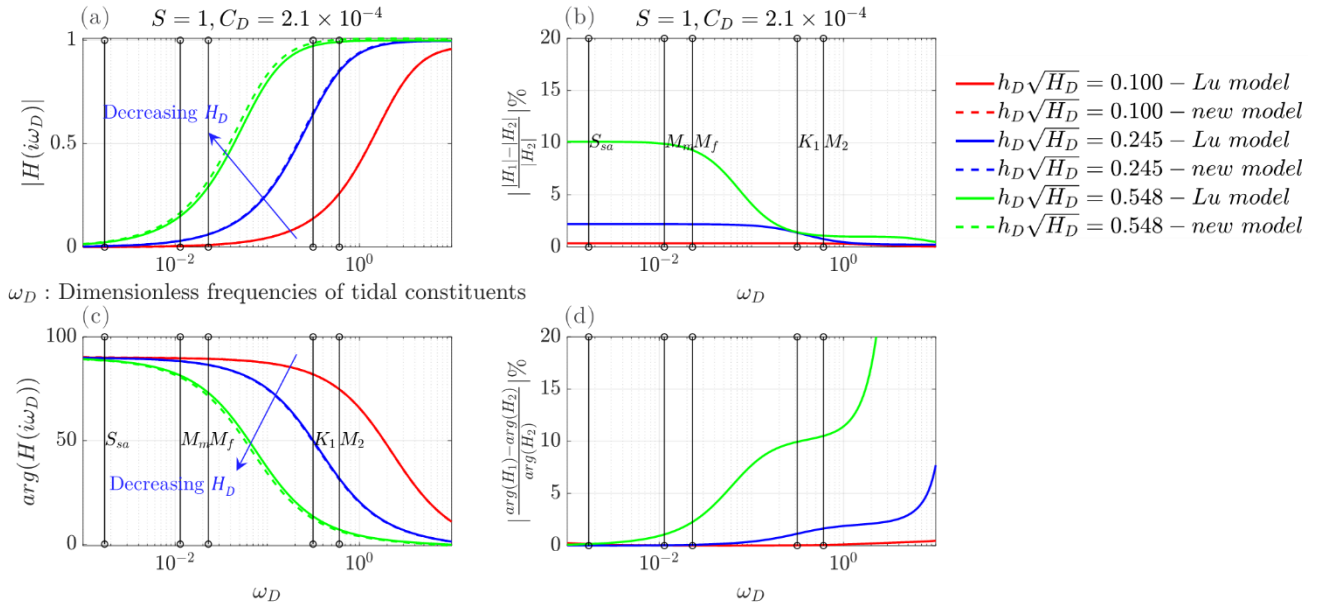427 in a vertical well.

428

Figure 5: Comparison between Lu's model and the new model under three different values of $h_D\sqrt{H_D}$. (a): the amplitude of the transfer functions; (b): the relative error in amplitude of the transfer functions between Lu's solution and the new solution; (c): the phase of the transfer functions; (d) the relative error in phase of the transfer functions between Lu's solution and the new solution. (S_{sa}: semiannual constituent; M_m: monthly constituent; M_f: Fortnightly constituent; K_1: diurnal constituent; M_2: semidiurnal constituent.)

**Table 3**: The absolute values of physical parameters to generate Figure 5

Parameters	Values	Parameters	Values
Well radius r_w	0.1 m	Aquifer	4×10^{-12} m^2
Viscosity μ	0.003 Pa·s	Aquitard	4×10^{-13} m^2
Porosity φ	0.25	Aquitard thickness	10,60,300 m
Compressibility c_t	1.02×10^{-9}	Skin S	1
Aquifer thickness b'	100 m	Wellbore storage C	2.3059×10^{-6} m^3 /Pa
Well length l	300 m		

436

4.3 Relative error variation with skin effect S, frequencies of tidal force, and thickness of aquifer

Figure 6 and Figure 7 illustrate the variation in relative errors between the approximate solutions and the new solutions with the skin effect (S), the frequencies of tidal force, and the nondimensional thickness of aquifer (h_D) for a vertical well and a horizontal well in a semiconfined aquifer respectively. Except for the skin effect and the thickness of aquifer, the values of other parameters align with those listed in Table 1 and Table 3.

These figures clearly demonstrate that the skin effect has negligible impact on the relative errors, while both the thickness of aquifer and the frequencies of tidal force exert significant influence on these errors. More precisely, an increase in aquifer thickness results in higher relative errors in both

447 the amplitude and phase of the transfer function. As for the frequencies of tidal force, a tidal constituent
448 with a high frequency leads to smaller relative errors in the amplitude of the transfer function but larger
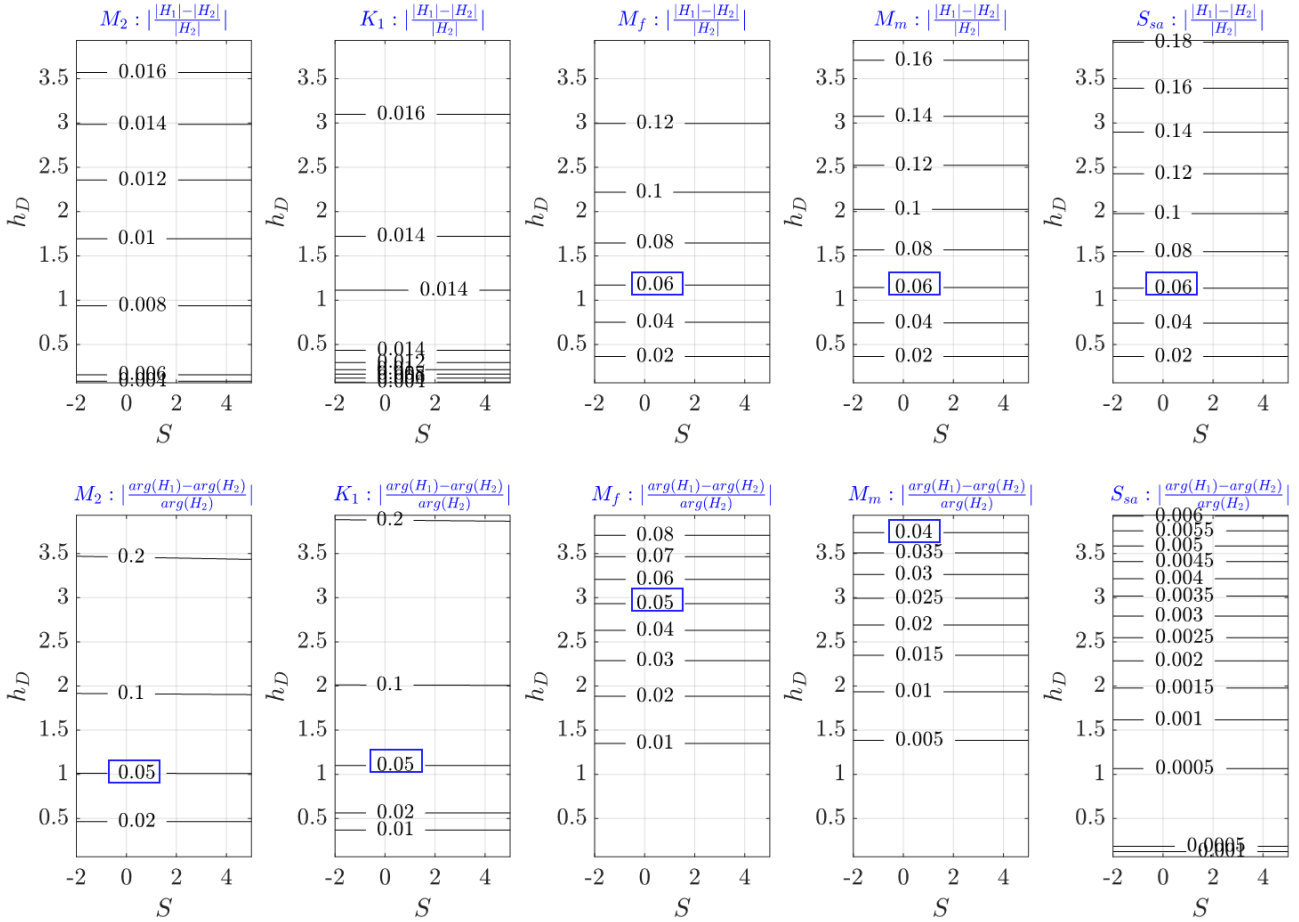449 errors in its phase.
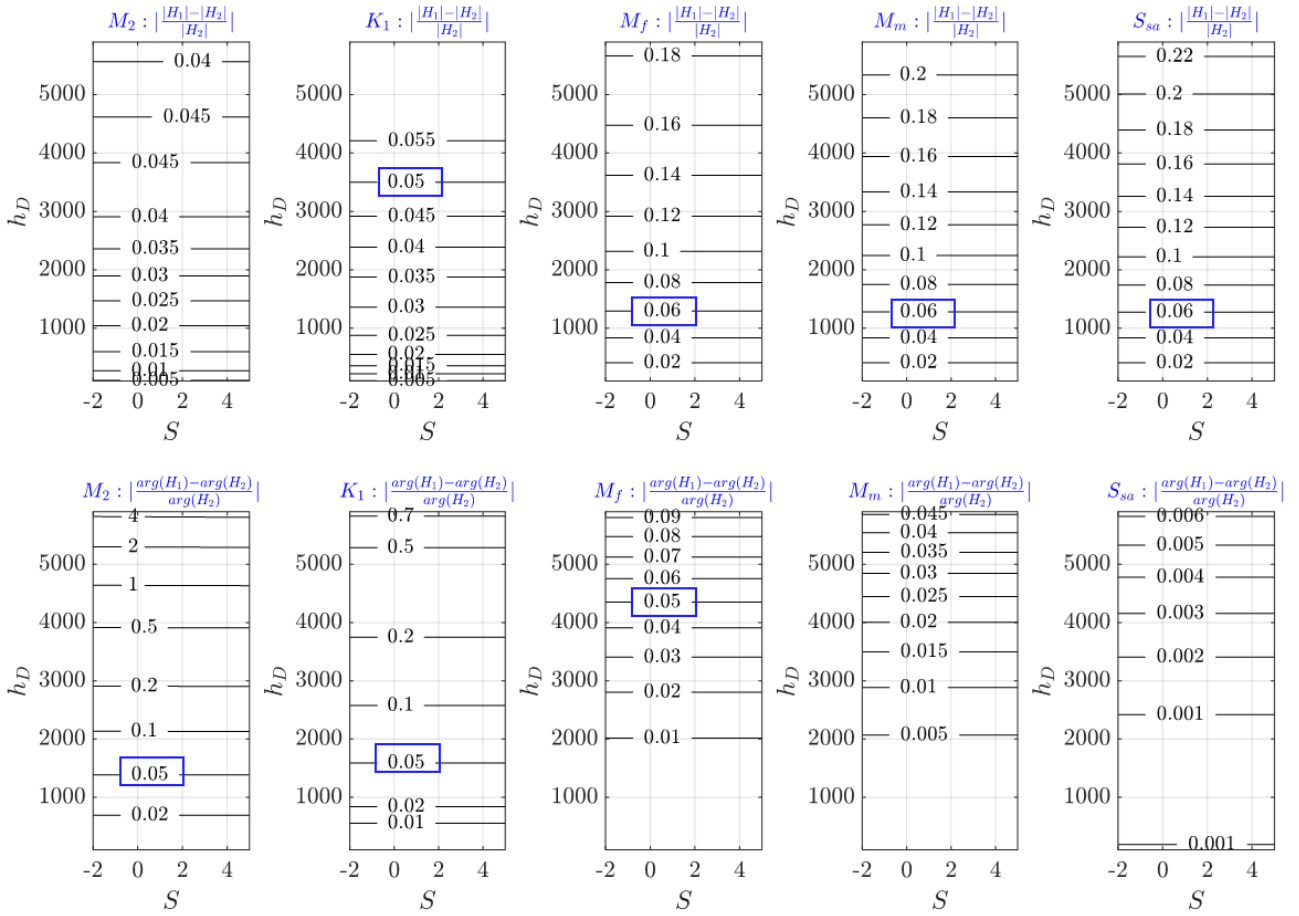
450
451 **Figure 6**: The variation in relative errors between the approximate solutions and the new solutions
452 with the skin effect (S), the frequencies of tidal force, and the nondimensional thickness of aquifer
453 (h_D) for a vertical well.

Figure 7: The variation in relative errors between the approximate solutions and the new solutions with the skin effect (S), the frequencies of tidal force, and the nondimensional thickness of aquifer (h_D) for a horizontal well.

4.4 The physical significance of the nondimensional number: $h_D\sqrt{H_D}$

Previously, the nondimensional number, either represented as $h_D\sqrt{H_D}$ or $\sqrt{\dfrac{hk'}{b'k}}$, was derived mathematically, where h and b' denote the thickness of the aquifer and overlaying layer, respectively, and k and k' symbolize their respective permeabilities. This nondimensional number forms the basis for a quantitative criterion to assess the applicability of the existing solutions derived from the approximate theory that is currently in use. The physical significance of this nondimensional number can be understood by looking at the fluid flows from the overlaying layer to the target aquifer, as shown in Figure 8(a). The fluid flow experiences two resistances: one for diffusion within the overlaying layer (proportional to its thickness b' and inversely proportional to its permeability k'), and the other for diffusion within the target aquifer (also proportional to its thickness h and inversely proportional to its permeability k). The nondimensional number $\sqrt{\dfrac{hk'}{b'k}}$ can be interpreted as the ratio between the flow resistances of the target aquifer and the overlaying layer. If the flow resistance within the overlaying layer is much greater than that within the target aquifer, the nondimensional number will be less than a specific value of 0.245, which has been derived mathematically in the previous

472   sections. In systems where the nondimensional number less than 0.245, it may be presumed that fluid
473   flows into the target aquifer have time to uniformly distribute and thus have uniform pressure along
474   the vertical direction, consequently, the leakage at the boundary can be approximated as a volumetric
475   source term. Conversely, for systems with the nondimensional number exceeding 0.245, which means
476   the flow resistance within the overlaying layer is not significantly greater or may even be less than that
477   within the target aquifer, pressure gradients within the target aquifer become important and the interior
478   of the target aquifer cannot be assumed to have uniform pressure along the vertical direction, rendering
479   the approximate theory invalid.

480   From another perspective, the nondimensional number $\sqrt{\frac{hk'}{b'k}}$ can be understood as a descriptor
481   for a physical system's ability to maintain uniform distribution against boundary effects, akin to the
482   role of the Biot number in heat transfer, as illustrated in Figure 8(b).   In this figure, the symbols h
483   and δ represent the characteristic length of the object and the thickness of thermal boundary layer,
484   respectively, and K and K' symbolize their respective thermal conductivities. The Biot number is
485   defined as $\mathrm{Bi} = \frac{h_c}{K}h$, signifying the ratio of the conductive heat resistance within the object to the
486   convective heat transfer resistance across the object's boundary. Here, h_c is the convective heat
487   transfer coefficient, K is the thermal conductivity of the object, and h is a characteristic length of
488   the object. After modeling the heat conduction within the thermal boundary layer, the convective heat
489   transfer coefficient can be expressed as $h_c = \frac{K'}{\delta}$, allowing the Biot number to be expressed as $\mathrm{Bi} =$
490    $\frac{h}{K}\frac{K'}{\delta}$, which takes exactly the same form with the nondimensional number $\sqrt{\frac{hk'}{b'k}}$ except for the
491   presence of the square root operator. Consequently, this number $\sqrt{\frac{hk'}{h'k}}$ can be named as the "hydraulic
492   Biot number" to emphasize its application in hydrology and to set it apart from the original Biot number,
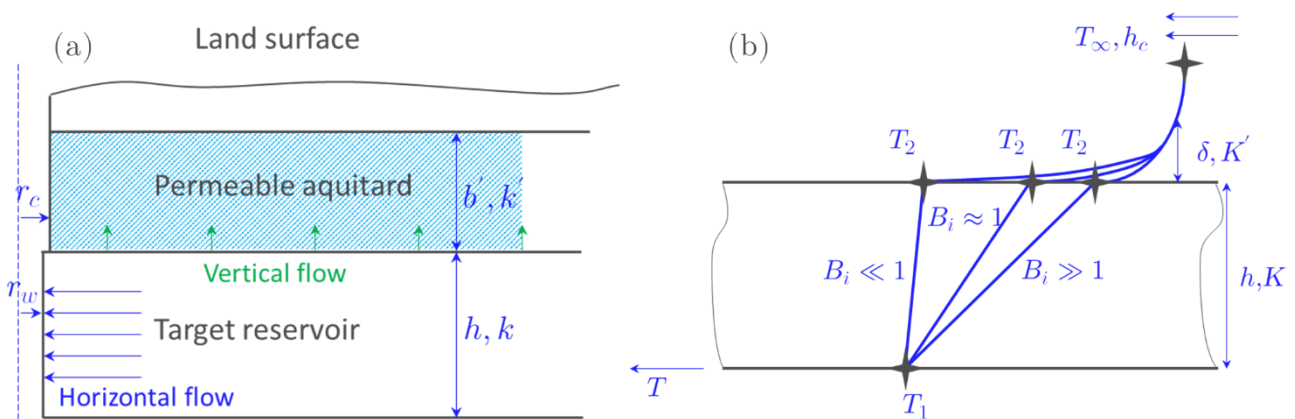493   which pertains to the field of heat transfer.

494

495   **Figure 8**: (a) the fluid flows from the overlaying layer to the target aquifer; (b) heat transfer from the
496   surface to the object.

497   **5. Examine the assumption: uniform flow rate along the wellbore**

498   In the previous section, it was concluded that the existing approximate solution exhibits

499 acceptable error and proves suitable only when the nondimensional number $\sqrt{\dfrac{hk'}{h'k}}$ is less than 0.245.

500 Our new solution extends this upper limitation by solving the standard diffusion equation with
501 appropriate initial and boundary conditions, expressing the leakage as a boundary condition. However,
502 both the approximate and new solutions are solved under the assumption of a uniform flow rate along
503 the wellbore. This assumption can be acceptable for a horizontal well because the horizontal well is
504 parallel to the leakage boundary while this assumption may not always be valid for a vertical well,
505 especially when the thickness of target aquifer is large and the permeability of the overlaying layer is
506 not low. Therefore, it becomes necessary to quantify when this assumption fails and the scope of
507 application for the new solution.

5.1 Two candidates: $h_D\sqrt{H_D}$ and k'/k

509 To quantify when the assumption of uniform flow rate fails, the initial step is to identify a
510 nondimensional number that can reflect the distribution of flow rate along the wellbore. Two potential
511 candidates were considered here. One is $h_D\sqrt{H_D}$ ($\sqrt{\dfrac{hk'}{h'k}}$), the "hydraulic Biot number" derived earlier.
512 The other is k'/k, the ratio of the permeability of the overlaying layer to that of the target aquifer.

513 Numerical experiments were then performed to pinpoint the appropriate nondimensional
514 number. Because the distribution of flow rate cannot be obtained directly from the new solution due to
515 the underlying assumption of uniform flow rate during the model's construction, the research
516 methodology shifted to that under the premise of assuming a uniform distribution of flow rate, the
517 focus is on investigating the pressure distribution along the wellbore. If the variation in pressure
518 distribution remains within 10%, the assumption of uniform flow rate distribution is considered correct;
519 otherwise, it is deemed incorrect.

520 Subsequently, the effects of varying $h_D\sqrt{H_D}$ and k'/k on wellbore pressure distribution are

521 explored under two extreme scenarios for a vertical well: $\dfrac{h_D}{b_D} = 0.048$ (very thin target aquifer

522 relative to the overlaying layer) and $\dfrac{h_D}{b_D} = 6$ (very thick target aquifer relative to the overlaying layer).

523 The results are presented in Figure 9. In this figure, the x-axes represent amplitude and phase of the
524 transfer function between wellbore pressure and Earth tides. Because the referenced Earth tides are
525 consistent, the amplitude and phase of the transfer function can serve as representations of the relative
526 amplitude and phase of the wellbore pressure. The y-axis indicates height from the well bottom. Each

527 curve corresponds to specific values of $h_D\sqrt{H_D}$ and k'/k, identifiable by the color in the color bar.

528 From Figure 10, it is observed that the phase of wellbore pressure remains nearly consistent from the
529 well bottom to wellhead, while the amplitude of wellbore pressure changes along the wellbore. Two

530 representative curves are highlighted: one with $h_D\sqrt{H_D} = 0.245$ and the other is marked with

531 $k'/k = 0.09$ or 0.1. Under both two extreme scenarios, a small "hydraulic Biot number" ($h_D\sqrt{H_D} =$

532 0.245) consistently maintains a pressure distribution close to uniform along the wellbore, while a small
533 value of k'/k (0.09 or 0.1) fails to ensure uniformity in the thick aquifer scenario. This illustrates
534 that the uniformity of pressure distribution can be controlled by the "hydraulic Biot number" instead
535 of k'/k. Thus, "hydraulic Biot number" is the key nondimensional number that reflects the
536 distribution of flow rate along the wellbore.
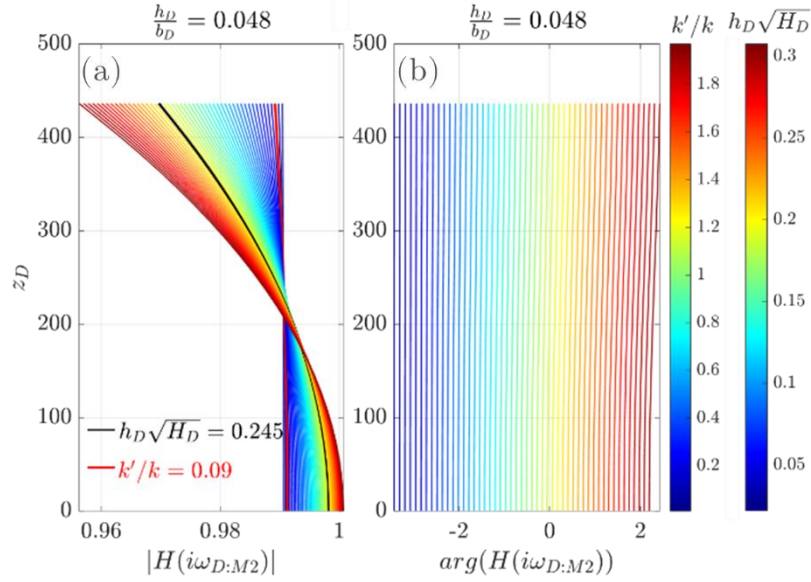

537

538 **Figure 9**: Wellbore pressure distribution under $\frac{h_D}{b_D} = 0.048$: (a) amplitude; (b) phase.
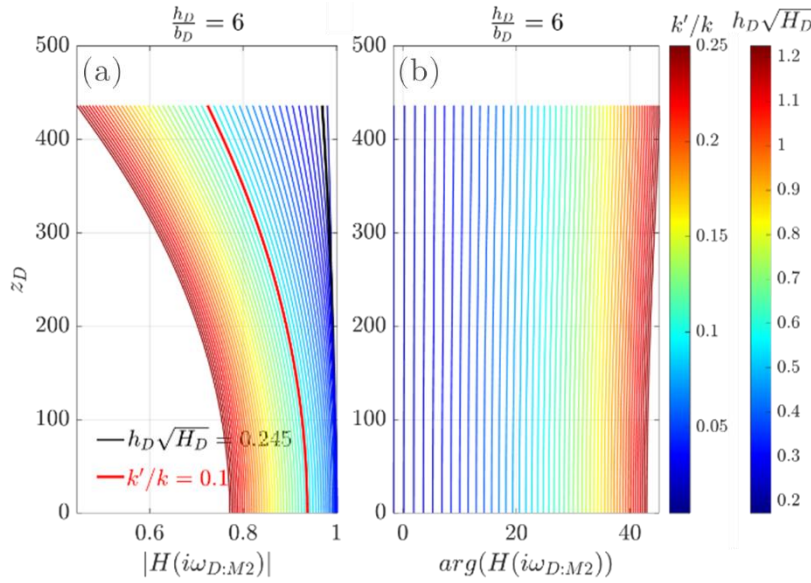

539

540 **Figure 10**: Wellbore pressure distribution under $\frac{h_D}{b_D} = 6$: (a) amplitude; (b) phase.

541 **5.2 The condition for the assumption of uniform flow rate along wellbore**

542 After determining the crucial nondimensional number that reflects the distribution of flow rate
543 along the wellbore, Figure 11 illustrates the amplitude ratios of wellhead pressure to well bottom
544 pressure variation with $h_D\sqrt{H_D}$, under different tidal constituents with varying frequencies

545   (semidiurnal M_2, diurnal K_1 and half month M_f) and different aquifer thickness ranging from $h_D = $
546   1 to 100.

547   From earlier discussions, if the variation in pressure distribution remains within 10% (the
548   amplitude ratio of wellhead pressure to well bottom pressure falls in the range of 0.9 to 1.1), the
549   assumption of uniform flow rate distribution is considered correct; otherwise, it is deemed incorrect.
550   Assuming $h^2/k > 10^{13}$, which holds true for most aquifers, two boundaries are determined. The
551   lower boundary, marked with a green curve in Figure 11, is determined when h^2/k is a large value.
552   The upper boundary, marked with a blue curve, is determined by $h^2/k = 10^{13}$. Two critical points,
553   labeled A and B, are determined by the intersections of the lines y=0.9 and y=1.1 with the two

554   boundaries. The minimum $h_D\sqrt{H_D}$ values of points A and B establish the upper limit where the

555   assumption of uniform flow rate distribution remains valid. With an increase in the tidal period (from

556   M_2 to M_f), the value of $h_D\sqrt{H_D}$ corresponding to point A remains constant at 0.475, while that

557   corresponding to point B decreases from around 0.8 to 0.3. This behavior occurs because the aquifer
558   tends to be more confined under tidal force with high frequency and tends to be more open under tidal
559   force with low frequency (Wang, 2000). A more open aquifer leads to a tighter upper limit where the
560   assumption of uniform flow rate distribution is valid. Because the amplitude of tidal constituent M_f
561   is too small, semidiurnal and diurnal tidal constituents are primarily analyzed to characterize the

562   aquifer. Thus, by comparing the $h_D\sqrt{H_D}$ values of lower and upper boundaries for semidiurnal and

563   diurnal tidal constituents, the upper limit for the assumption of uniform flow rate distribution is

564   identified as $h_D\sqrt{H_D} = 0.475$.
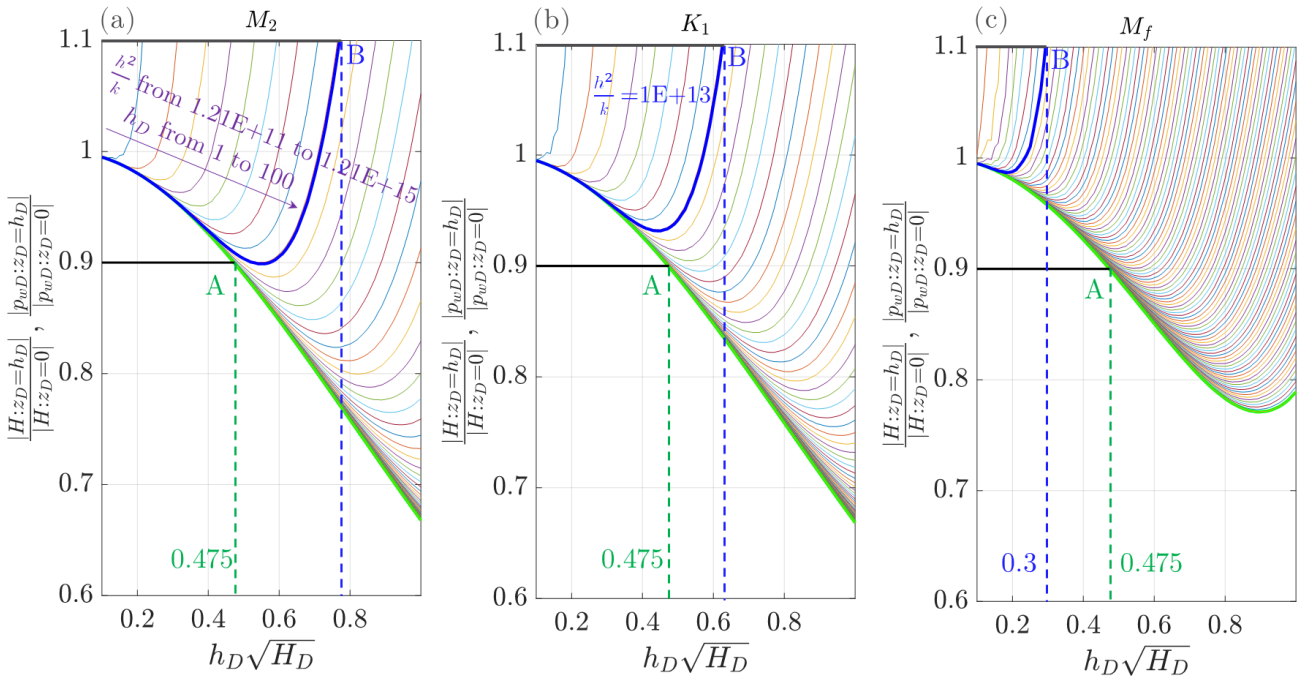

565

566   **Figure 11**: The amplitude ratios of wellhead pressure to well bottom pressure variation with

567    $h_D\sqrt{H_D}$: (a) semidiurnal constituent; (b) diurnal constituent; (c) half-month constituent.

568   In summary, the quantitative conditions for the application of both the approximate solution
569   and the new solution are detailed in Table 4. For a vertical or horizontal well in a semiconfined aquifer,

570   the approximate solution works only when $h_D\sqrt{H_D} < 0.245$. Meanwhile, the new solution is valid

571   when $h_D\sqrt{H_D} < 0.475$ for a vertical well and is always valid for a horizontal well. It is noted that

572   when $h_D\sqrt{H_D} \geq 0.475$, there is no existing analytical solution that works for a vertical well.

573   **Table 4**: The quantitative conditions for the application of both the approximate solution and the new
574   solution

	$h_D\sqrt{H_D} < 0.245$	$0.245 \leq h_D\sqrt{H_D} < 0.475$	$h_D\sqrt{H_D} \geq 0.475$
Vertical wells	Approximate solution/ New solution	New solution	No existing solution
Horizontal wells	Approximate solution/ New solution	New solution	New solution

575

6. Application of the new leaky aquifer model to the Arbuckle Aquifer, Oklahoma

577   The new solution was applied to the Arbuckle aquifer to illustrate its enhanced validity
578   compared to the existing one. Wang et al. (2018) developed the current semiconfined model and
579   applied it to assess the vertical leakage of the Arbuckle aquifer. The data analyzed in their study was
580   collected from a deep monitoring well in the Arbuckle aquifer in Oklahoma by the US Geological
581   Survey. Table 5 provides detailed information on both the well and the aquifer parameters to
582   characterize this specific well-aquifer system. According to Wang's findings, there is a $12.5°$ phase
583   advance between the water level tidal response and the theoretical tide. Given the thickness of the
584   aquitard (277m) and the storativity of the aquifer ranging from 2.6×10^{-6} to 2.7×10^{-5}, the estimated
585   hydraulic conductivity of the aquitard is between 3×10^{-8} to 3×10^{-7} m/s, based on the existing
586   approximate semiconfined model. Consequently, the permeability of the aquitard is estimated to be
587   around 3×10^{-15} to 3×10^{-14} m^2.

588   **Table 5**: Details parameters to characterize the Arbuckle aquifer

Parameters	Values	Parameters	Values
Well depth	960m	Well radius	11cm
Casing radius	3.65cm	Thickness of aquitard	277m
Thickness of aquifer	48m	Permeability	2×10^{-14} to 3×10^{-12} m^2
Transmissivity	9.6×10^{-6} to 1.4×10^{-3} m^2/s	Storativity	2.6×10^{-6} to 2.7×10^{-5}

589

590   Given the permeabilities and thickness of both the aquifer and aquitard, the "hydraulic Biot

591   number" $h_D\sqrt{H_D}$ can be calculated, as shown in Figure 12(a). In this figure, the white area represents

592   the "hydraulic Biot number" less than 0.245, indicating that both the existing approximate solution

593   and the new solution are applicable within this region. However, in the blue area where the "hydraulic

594   Biot number" exceeds 0.245, the new solution should be analyzed in preference to the existing

595   approximation, although this blue area represents a relatively small region.

596   A value of $h_D\sqrt{H_D}$ is selected from the blue area, marked with a red star. With given values

597   for the aquifer's permeability and the estimated aquitard's permeability, this value of $h_D\sqrt{H_D}$ is

598   around 0.4. Both the existing and the new solutions are applied to this specific case. The corresponding

599   phase advance variations with leakage coefficients are shown in Figure 12(b) and the relative errors of

600   phase advance between the existing and new models are shown in Figure 12(c). In these figures, the

601   red line represents the result of Gao and Wang's model, while the blue line corresponds to the new

602   model. The intersection points between these two lines and the black horizontal line (which represents

603   the phase advance equal to 12.5°) result in two leakage coefficients: 1.1×10^{-6} and 1.2×10^{-6},

604   corresponding to the existing and new models, respectively. The relative error in phase advance

605   between these two models is around 10% given the estimated leakage coefficient and the relative error

606   in estimated leakage coefficients between these two models is about 9% given the phase advance equal

607   to 12.5°. Although a 10% error is not a major error, these results nonetheless highlight the enhanced

608   validity of the new solution compared to the existing one and expand the applicability of tidal analysis

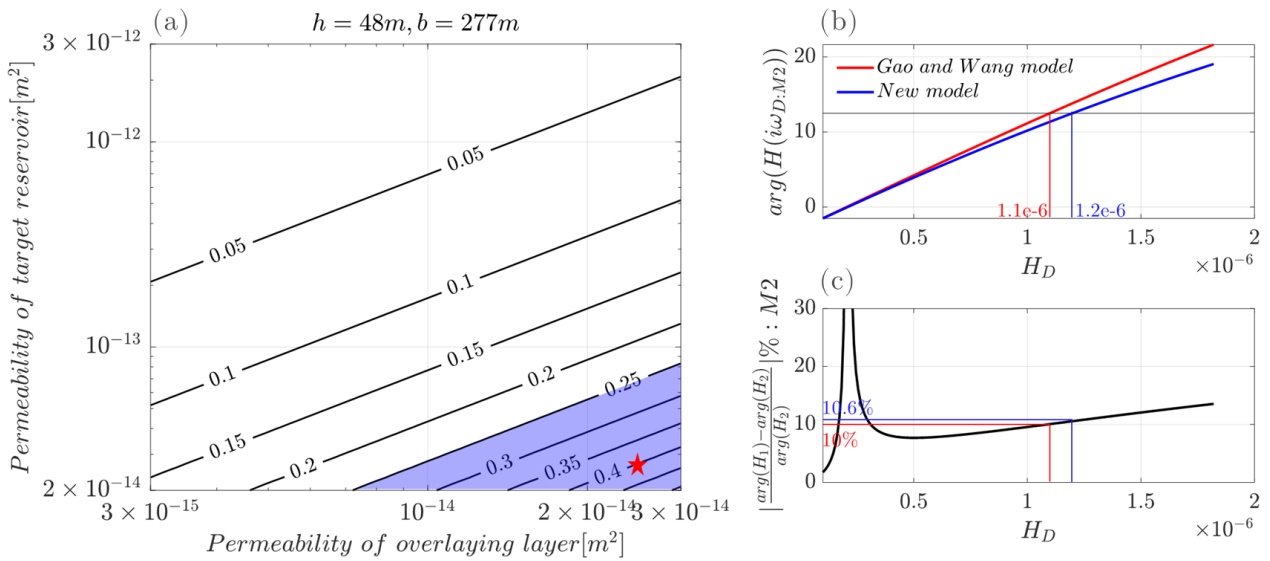609   to aquifers with relatively large thickness and leakage.

610

611   **Figure 12**: (a) the "hydraulic Biot number" $h_D\sqrt{H_D}$ for the Arbuckle aquifer; (b) phase advance

612   variations with leakage coefficients when $h_D\sqrt{H_D} = 0.41$; (c) relative errors of phase advance

613   between the existing and new models when $h_D\sqrt{H_D} = 0.41$.

614   **7. Summary and Conclusions**

615   Our work can be summarized as follows:

1. Accurate solutions for tidal behaviors of a vertical well and a horizontal well in aquifers with relatively large thickness and leakage were obtained by solving the standard diffusion equation with appropriate initial and boundary conditions, expressing the leakage as a boundary condition instead of treating it as a volumetric source term in the diffusion equation. The difference between this solution and that of Hantush (1967) is that Hantush analyzed the pump test results and did not take the tidal force into consideration.

2. The "hydraulic Biot number" was derived mathematically, dependent on the thickness of the aquifer and overlying layer, as well as their respective permeabilities and expressed as $h_D\sqrt{H_D}$.

   This nondimensional number "hydraulic Biot number" forms the basis for a quantitative criterion to assess the applicability of the existing approximate solution. The physical significance of this number was discussed and it can be understood as a descriptor for a physical system's ability to maintain uniform distribution against boundary effects, akin to the role of the Biot number in heat transfer.

3. Two key assumptions used in the existing approximate solution are assessed: one is relative thin aquifer and relative low permeability of aquitard and the other is uniform flow rate along wellbore. The quantitative criterion of the applicability of both the existing solution and the new solution were concluded. In the case of a vertical well, the existing solution exhibits acceptable error and proves suitable only the nondimensional number is less than 0.245. Our new solution extends this upper limitation to 0.475. However, when the number is greater than 0.475, both the existing solution and our new solution are invalid due to the invalid uniform flow rate assumption. For a horizontal well, when the number is less than 0.245, the existing solution is suitable with acceptable error. Our new solution effectively overcomes this limitation.

4. The new solution and existing solution were applied to the case of the Arbuckle aquifer to demonstrate the improved validity of the new solution compared to the existing one.

Acknowledgements

References

Agnew, D. C. (2012). SPOTL: Some programs for ocean-tide loading. Technical Report, Scripps Institution of Oceanography.

Allègre, V., Brodsky, E. E., Xue, L., Nale, S. M., Parker, B. L., & Cherry, J. A. (2016). Using earth-tide induced water pressure changes to measure in situ permeability: A comparison with long-term pumping tests. Water Resources Research, 52(4), 3113-3126. http://doi.org/10.1002/2015WR017346

Arditty, P. C., Ramey Jr, H. J., Nur, A. M.(1978). Response of a closed well reservoir system to stress induced by earth tides. Paper Number: SPE-7484-MS, SPE Annual Fall Technical Conference and Exhibition. Society of Petroleum Engineers. http://doi.org/10.2118/7484-MS

656 Bredehoeft, J. D. (1967). Response of well-aquifer systems to earth tides. Journal of Geophysical
657   Research, 72(12), 3075–3087. http://doi.org/10.1029/JZ072i012p03075

658 Burbey, T. J. (2010). Fracture characterization using Earth tide analysis. Journal of Hydrology, 380(3-
659   4), 237-246. https://doi.org/10.1016/j.jhydrol.2009.10.037

660 Burbey, T. J., Hisz, D., Murdoch, L. C., & Zhang, M. (2012). Quantifying fractured crystalline-rock
661   properties using well tests, earth tides and barometric effects. Journal of Hydrology, 414, 317-328.
662   https://doi.org/10.1016/j.jhydrol.2011.11.013

663 Cutillo, P. A., & Bredehoeft, J. D. (2011). Estimating aquifer properties from the water level response
664   to earth tides. Groundwater, 49(4), 600-610. https://doi.org/10.1111/j.1745-6584.2010.00778.x

665 Dean, G., Hardy, R., and Eltvik, P. (1994). Monitoring compaction and compressibility changes in
666   offshore chalk reservoirs. SPE Formation Evaluation, 9(01):73–76. http://doi.org/10.2118/23142-
667   PA

668 Doan, M. L., Brodsky, E. E., Prioul, R., & Signer, C. (2006). Tidal analysis of borehole pressure-A
669   tutorial. University of California, Santa Cruz, 25, 27.

670 Gao, X., Sato, K., & Horne, R. N. (2020). General solution for tidal behavior in confined and
671   semiconfined aquifers considering skin and wellbore storage effects. Water Resources Research,
672   56(6), e2020WR027195. http://doi.org/10.1029/2020WR027195

673 Gieske, A., & De Vries, J. J. (1985). An analysis of earth-tide-induced groundwater flow in eastern
674   Botswana. Journal of Hydrology, 82(3-4), 211–232. http://doi.org/10.1016/0022-1694(85)90018-
675   6

676 Hantush, M. S. (1960). Modification of the theory of leaky aquifers. Journal of Geophysical
677   Research, 65(11), 3713-3725. http://doi.org/10.1029/JZ065i011p03713

678 Hantush, M. S. (1967). Flow of groundwater in relatively thick leaky aquifers. Water Resources
679   Research, 3(2), 583-590. http://doi.org/10.1029/WR003i002p00583

680 Horne, R. N. (1995). Modern well test analysis. Petroway, Inc.

681 Hsieh, P. A., Bredehoeft, J. D., & Farr, J. M. (1987). Determination of aquifer transmissivity from
682   Earth   tide   analysis.   Water   resources   research,   23(10),   1824-1832.
683   http://doi.org/10.1029/WR023i010p01824

684 Jacob, C. E. (1939). Fluctuations in artesian pressure produced by passing railroad-trains as shown in
685   a well on Long Island, New York. Eos, Transactions American Geophysical Union, 20(4), 666-
686   674. http://doi.org/10.1029/TR020i004p00666

687 Lai, G., Ge, H., Xue, L., Brodsky, E. E., Huang, F., & Wang, W. (2014). Tidal response variation and
688   recovery following the Wenchuan earthquake from water level data of multiple wells in the
689   nearfield. Tectonophysics, 619, 115-122. https://doi.org/10.1016/j.tecto.2013.08.039

690 Liang, X., Wang, C. Y., Ma, E., & Zhang, Y. K. (2022). Effects of unsaturated flow on hydraulic head
691   response to Earth tides–An analytical model. Water Resources Research, 58(2), e2021WR030337.
692   https://doi.org/10.1029/2021WR030337

693 Lu, X., Sato, K., & Horne, R. N. (2022, September). Analysis of Tidal Behavior of a Horizontal Well

694   to Determine Reservoir Properties. Paper SPE-210166-MS presented at the SPE Annual Technical
695   Conference and Exhibition, October 3–5, 2022. http://doi.org/10.2118/210166-MS

696 Matsumoto, K., Sato, T., Takanezawa, T., & Ooe, M. (2001). GOTIC2: A program for computation of
697   oceanic tidal loading effect. Journal of the Geodetic Society of Japan, 47(1), 243-248.

698 McMillan, T. C., Rau, G. C., Timms, W. A., & Andersen, M. S. (2019). Utilizing the impact of Earth
699   and atmospheric tides on groundwater systems: A review reveals the future potential. Reviews of
700   Geophysics, 57(2), 281-315. http://doi.org/10.1029/2018RG000630

701 Melchior, P. (1966). The tides of the planet earth. Pergamon Press, Oxford.

702 Merritt, M. L. (2004). Estimating hydraulic properties of the Floridan aquifer system by analysis of
703   earth-tide, ocean-tide, and barometric effects, Collier and Hendry Counties, Florida. Reston, VA:
704   US Department of the Interior, US Geological Survey.

705 Rau, G. C., McMillan, T. C., Andersen, M. S., & Timms, W. A. (2022). In situ estimation of subsurface
706   hydro-geomechanical properties using the groundwater response to semi-diurnal Earth and
707   atmospheric tides. Hydrology and Earth System Sciences, 26(16), 4301-4321.
708   http://doi.org/10.5194/hess-26-4301-2022

709 Robinson, E. S., & Bell, R. T. (1971). Tides in confined well-aquifer systems. Journal of Geophysical
710   Research, 76(8), 1857–1869. http://doi.org/10.1029/JB076i008p01857

711 Rojstaczer, S., & Agnew, D. C. (1989). The influence of formation material properties on the response
712   of water levels in wells to Earth tides and atmospheric loading. Journal of Geophysical Research:
713   Solid Earth, 94(B9), 12403-12411. https://doi.org/10.1029/JB094iB09p12403

714 Sato, K. (2006). Monitoring the underground migration of sequestered carbon dioxide using Earth
715   tides. Energy conversion and management, 47(15-16), 2414-2423.
716   http://doi.org/10.1016/j.enconman.2005.11.005

717 Sato, K., & Horne, R. N. (2018). Time-lapse analysis of pressure transients due to ocean tides for
718   estimating CO2 saturation changes. International Journal of Greenhouse Gas Control, 78, 160-167.
719   http://doi.org/10.1016/j.ijggc.2018.08.005

720 Sato, K., Tamura, Y., Osato, K., & Horne, R. N. (2022). Assessing poroelastic properties of a
721   geothermal reservoir by tidal signal analysis. Geothermics, 100, 102352.
722   http://doi.org/10.1016/j.geothermics.2022.102352

723 Simon, J. B., Fulton, P. M., & Xue, L. (2021). Hydrogeologic property estimation in plate boundary
724   observatory boreholes using tidal response analysis. Geofluids, 2021, 1-19.
725   https://doi.org/10.1155/2021/6697021

726 Skempton, A. W. (1954). The pore-pressure coefficients A and B. Geotechnique, 4(4), 143-147.
727   http://doi.org/10.1680/geot.1954.4.4.143

728 Thambynayagam, R. K. (2011). The diffusion handbook: applied solutions for engineers. New York:
729   McGraw-Hill Professional.

730 Valois, R., Rau, G. C., Vouillamoz, J. M., & Derode, B. (2022). Estimating hydraulic properties of the
731   shallow subsurface using the groundwater response to Earth and atmospheric tides: A comparison
732   with pumping tests. Water Resources Research, 58(5), e2021WR031666.

733   http://doi.org/10.1029/2021WR031666

734 Van der Kamp, G., & Gale, J. E. (1983). Theory of earth tide and barometric effects in porous
735   formations with compressible grains. Water Resources Research, 19(2), 538-544.
736   http://doi.org/10.1029/WR019i002p00538

737 Wang, C. Y., Doan, M. L., Xue, L., & Barbour, A. J. (2018). Tidal response of groundwater in a leaky
738   aquifer—Application to Oklahoma. Water Resources Research, 54(10), 8019-8033.
739   http://doi.org/10.1029/2018WR022793

740 Wang, H. F. (1993). Quasi-static poroelastic parameters in rock and their geophysical applications.
741   Pure and Applied Geophysics, 141, 269-286. http://doi.org/10.1007/BF00998332

742 Wang, H. F. (2000). Theory of linear poroelasticity with applications to geomechanics and
743   hydrogeology (Vol. 2). Princeton University Press. http://doi.org/10.1515/9781400885688

744 Xue, L., Li, H. B., Brodsky, E. E., Xu, Z. Q., Kano, Y., Wang, H., Mori, J. J., Si, J. L., Pei, J. L., Zhang,
745   W., Yang, G., Sun, Z. M., and Huang, Y. (2013). Continuous permeability measurements record
746   healing inside the Wenchuan earthquake fault zone. Science, 340(6140):1555–1559.
747   https://doi.org/10.1126/science.1237237

748 Zhang, Y., Wang, C. Y., Fu, L. Y., & Yang, Q. Y. (2021). Are deep aquifers really confined? Insights
749   from deep groundwater tidal responses in the North China Platform. Water Resources Research,
750   57(11), e2021WR030195. https://doi.org/10.1029/2021WR030195

751 Zhu, A. Y., & Wang, C. Y. (2020). Response of leaky aquifers to Earth tides–Interpreted with numerical
752   simulation. Journal of Hydrology, 581, 124458. https://doi.org/10.1016/j.jhydrol.2019.124458